

PAPER

# Integrated core-SOL modelling of fuelling, density control and divertor heat loads for the flat-top phase of the ITER H-mode D-T plasma scenarios

To cite this article: L. Garzotti *et al* 2019 *Nucl. Fusion* **59** 026006

View the [article online](#) for updates and enhancements.

## Recent citations

- [Compatibility of pellet fuelling with ELM suppression by RMPs in the ASDEX Upgrade tokamak](#)  
M. Valovi *et al*
- [Modelling one-third field operation in the ITER pre-fusion power operation phase](#)  
M. Schneider *et al*



**IOP | ebooks™**

Bringing together innovative digital publishing with leading authors from the global scientific community.

Start exploring the collection—download the first chapter of every title for free.

# Integrated core-SOL modelling of fuelling, density control and divertor heat loads for the flat-top phase of the ITER H-mode D-T plasma scenarios

L. Garzotti<sup>1</sup>, P. Belo<sup>1</sup>, G. Corrigan<sup>1</sup>, D. Harting<sup>1</sup>, F. Köchl<sup>1</sup>, A. Loarte<sup>2</sup>, E. Militello Asp<sup>1</sup>, V. Parail<sup>1</sup>, R. Ambrosino<sup>3</sup>, M. Cavinato<sup>5</sup>, M. Mattei<sup>4</sup>, M. Romanelli<sup>1</sup>, R. Sartori<sup>5</sup> and M. Valovič<sup>1</sup>

<sup>1</sup> CCFE, Culham Science Centre, OX14 3DB Abingdon, United Kingdom of Great Britain and Northern Ireland

<sup>2</sup> ITER Organization, Route de Vinon-sur-Verdon, 13067 St Paul Lez Durance, France

<sup>3</sup> CREATE, University of Naples 'Federico II', Naples, Italy

<sup>4</sup> CREATE, University of Campania 'Luigi Vanvitelli', Naples, Italy

<sup>5</sup> Fusion For Energy Joint Undertaking, Josep Pla 2, 08019, Barcelona, Spain

E-mail: [luca.garzotti@ukaea.uk](mailto:luca.garzotti@ukaea.uk)

Received 4 May 2018, revised 28 September 2018

Accepted for publication 22 November 2018

Published 19 December 2018



## Abstract

The operation of a tokamak designed to test the sustainability of a thermonuclear grade plasma like the international tokamak experimental reactor (ITER) presents several challenges. Among them is the necessity of fuelling the plasma to reach the density required to generate enough fusion power to achieve  $Q = 10$  and, at the same time, to avoid excessive power loads at the divertor targets (beyond  $10 \text{ MW m}^{-2}$ ). Whether this goal is achievable or not depends on the details of the fuelling scheme, of the atomic species that are injected into the plasma, of the power radiation pattern in the scrape-off layer and in the divertor, of the additional heating schemes and of the transport mechanisms at work in the core and near the edge of the plasma.

In this study we present, for different operational scenarios, the results of an integrated modelling approach to the problem taking into account all the different aspects of it, albeit with some limitations and simplifications discussed in the paper. The tool adopted for our simulations is the JINTRAC suite of codes, which can simulate in an integrated fashion the transport of particles and heat in different regions of the plasma.

Within the limitation of our modelling our assessment is that, by carefully tuning the gas fuelling and impurity seeding, it is indeed possible for ITER to achieve  $Q = 10$  and at the same time maintain acceptable divertor power loads. We also investigate the sensitivity of this result to some of the uncertainties in the modelling assumptions underlying the simulations presented in the paper.

Keywords: tokamak, ITER, density, fuelling, divertor, integrated modelling, impurity seeding

(Some figures may appear in colour only in the online journal)

## 1. Introduction

The fuelling and the control of the plasma density in ITER present many challenges and uncertainties. The high density and temperature at the separatrix will almost certainly make the scrape-off layer (SOL) opaque to the neutral penetration and the fuelling by means of gas puff less efficient than in present-day experiments [1]. Therefore, depending on the transport characteristics of the SOL and the pedestal, other methods such as, for example, pellet injection could be required to reach the target core density during the different phases of the discharge. In addition, the power flowing through the SOL will have to be reduced in order to avoid excessive power fluxes on divertor target plates, but, at the same time, be high enough to maintain partial attachment and avoid the onset of thermal instabilities like a MARFE (multifaceted asymmetric radiation from the edge). To model this problem comprehensively and self-consistently, it is necessary to take an integrated approach including the description of the core plasma, the SOL and the interaction with the first wall and the divertor plates. These simulations have been the focus of a modelling activity carried on within the framework of an ITER Task Agreement (C19TD51FE) implemented by Fusion for Energy under Grant GRT-502 and some general results regarding different phases of an ITER baseline pulse (L-mode, current ramp-up, L-H transition, H-mode, H-L transition and current ramp-down and termination) have been reported in [2] and [3] both for the non-active (H and He) and active (D and D-T) phase of ITER operations.

In this paper we build on previous results, but we concentrate on the flat-top of a D-T H-mode ITER plasma and present the results of detailed fully integrated core-SOL simulations of fuelling and density control at different currents, fields and levels of additional power. The material is organized as follows: in section 2 we describe the main modelling assumptions underlying the study, in section 3–6 we present the results at 5 MA, 7.5 MA, 10 MA and 15 MA respectively (including scans performed to address particular aspects of the physics involved and to test the sensitivity of the results to the modelling assumptions), in section 7 we discuss the results obtained in the simulations and in section 8 we summarize the main conclusions of the work including the sensitivity to parameters affected by significant uncertainty.

## 2. Description of the simulations

The simulations presented in this study were performed with the JINTRAC suite of codes developed at JET [4], which allows to run JETTO/SANCO (for main ion and impurity core transport), EDGE2D (for main ion and impurity SOL transport) and EIRENE (neutral transport) in a coupled fashion. The equations coupled between JETTO/SANCO and EDGE2D are the equations for the main ion and impurity density and the ion and electron temperature. The parallel momentum equation is solved in EDGE2D with zero parallel velocity at the separatrix as boundary condition, but not solved (and therefore not coupled) in JETTO/SANCO.

A substantial difference between previous studies [5–14] and the study presented in this paper consists in the fact that previous simulations of the SOL were performed by imposing the plasma parameters at the separatrix as boundary conditions, unlike here, where the whole plasma is modelled self-consistently and the plasma parameters at the separatrix are the result of the SOL dynamics, which, in turn, is determined by the evolution of the core plasma.

Numerically this is achieved by running simultaneously EDGE2D/EIRENE and JETTO/SANCO. In particular, with boundary conditions at the separatrix provided by JETTO/SANCO, EDGE2D/EIRENE is run for one time step, the duration of which is set by the rate of change of the plasma parameters (typically a few  $\mu\text{s}$ ). Subsequently JETTO/SANCO is advanced by the same time step with boundary conditions provided by a poloidal average of the EDGE2D/EIRENE solution and the cycle is repeated. In this way it is automatically guaranteed that, at the separatrix, the values of the fluxes and all the coupled plasma parameters are the same in EDGE2D/EIRENE and JETTO/SANCO during the whole simulation. For a plasma with few or light impurities, the computational cost of the numerical scheme described above is shared approximately equally between EDGE2D and EIRENE, JETTO/SANCO taking only a small fraction of the CPU time. However, when the number and the atomic weight of the impurities is increased the computational burden imposed by EDGE2D starts to dominate due to the increased number of equations.

In our simulations the core transport is split between neoclassical and anomalous. The neoclassical transport for main gas and impurities is modelled by NCLASS [15], whereas the anomalous transport is calculated with the Bohm/gyro-Bohm transport model [16]. This choice was dictated by the relatively low computational burden and the excellent numerical stability of the Bohm/gyro-Bohm transport model. However, to take into account a collisionality-dependent inward particle pinch present in more advanced physics based models, such as, for example, GLF23 [17], the Bohm/gyro-Bohm model was modified with the addition of a convective velocity  $v_{\text{inw}}$  of the form  $v_{\text{inw}}(\nu^*) = f(\nu^*) 0.5 D r/a^2$  where  $D$  is the cross-field particle diffusivity as defined, for example, in [19],  $\nu^*$  is the normalized electron collisionality and  $f(\nu^*) = \min(1, \exp(1 - \nu^*/\nu_{\text{th}}))$ . We fitted the constant  $\nu_{\text{th}} = 0.04$  by matching the density profiles obtained in Bohm/gyro-Bohm transport simulations for ITER at different current and field with the density profiles obtained in GLF23 transport simulations in identical conditions.

The transport in the edge transport barrier (ETB) is treated by the continuous ELM model described in [18], which mimics the limiting effect of the ELMs on the pressure gradient in the ETB by introducing additional transport averaged over time and clamps the normalized pressure gradient in the ETB,  $\alpha$ , at a prescribed critical value,  $\alpha_c$ . The height and the width of the pedestal (and, therefore,  $\alpha_c$ ) are estimated according to the EPED1 model [20] on the basis of peeling-ballooning stability and a proportionality between pedestal width and  $\sqrt{\beta_p}$ .

To describe the perpendicular transport in the far SOL we have assumed constant transport coefficients based on existing modelling of JET L-mode plasmas [21, 22]. Typical values used in this study are  $D_{\text{SOL}} = 0.3 \text{ m}^2 \text{ s}^{-1}$  and  $\chi_{\text{SOL},i,e} = 1.0 \text{ m}^2 \text{ s}^{-1}$ . A sensitivity study of the simulation results to the details of the perpendicular transport in the far SOL was conducted for the ITER L-mode and can be found in [23]. Near the separatrix in the SOL the transport coefficients are determined by the continuous ELM model. In this paper we present a sensitivity analysis to the extension of the region of reduced SOL transport in H-mode. Drifts were not taken into account in the simulations of the SOL dynamics.

The particle sources considered in this study were neutral beam ionization, gas puff, wall recycling and pellet injection. The neutral beam particle source is calculated by the PENCIL code [24]. Gas puff and wall recycling are treated inside the Monte Carlo code EIRENE [25]. The pellet source can be treated in a simplified way by the continuous pellet model, whereby an additional time-averaged particle source with a Gaussian radial profile is introduced in the density transport equation. The centre and the width of the Gaussian, which approximate the pellet deposition profile, and the intensity of the source, which is linked to the pellet particle throughput, are prescribed as input parameters. It is clear that this simplified model does not capture the intermittent nature of pellet injection. A more realistic description of the pellet source is given by the ablation/deposition code HPI2, which treats simultaneously the evaporation of the pellet and the fast transport associated with the drift of the dense and cold plasmoid surrounding the pellet [26] and can be used to calculate an instantaneous (i.e. not time-averaged) particle source every time a pellet is injected in the plasma. The particle sink due to the divertor pumping is modelled as a segment of the first wall located at the base of the divertor with albedo 0.97, in line with previous ITER simulations [1]. The resulting pumping speeds are in line with the values expected on ITER and reported in [27].

The heat sources associated with neutral beam injection (NBI) were calculated with PENCIL and the heat sources associated with ion and electron cyclotron resonance heating (ICRH and ECRH) were taken into account by prescribing fixed power deposition profiles obtained from stand alone calculations.

The composition of the core plasma was self-consistently calculated by the Bohm/gyro-Bohm transport model assuming a 50–50 D-T influx at the separatrix, with Be as main impurity coming from the first wall and Ne resulting from the seeding needed to radiate in the SOL part of the power crossing the separatrix and mitigate the divertor power load. In the SOL, however, because the version of EDGE2D used in this study was not able to simulate a two-species main plasma, we prescribed a pure D plasma with Be and Ne as impurities. In general, we did not include He in the plasma composition, although for some specific cases at 15 MA, presented in sections 6.5 and 6.6, we did run JINTRAC with He included in the impurity mix. We considered D and Ne as recycling species

(reflection coefficient equal to 1) and Be as sticky (reflection coefficient equal to 0). The ratio of atomic to molecular reflection was taken from the TRIM database inside EIRENE.

The plasma facing materials were assumed to be Be for the wall and W for the divertor. However, it should be noted that some initial simulations reported here were obtained with a Be divertor. This can be justified as representative of the limiting case in which the divertor is deposition dominated and the W target is covered by Be. Changing from a Be to a W divertor in the simulations, we modified the recycling properties of the plasma at the divertor and we eliminated the Be produced by sputtering, which can contribute to divertor radiation in the case of a Be divertor. In any case, because of the computational burden imposed on the computation of the SOL dynamics the transport of W was not taken into account in the simulations presented in this paper.

### 3. Results at 5MA

The fuelling of an ITER D-T H-mode plasma at 5 MA, 5.3 T and 53 MW of additional power (33 MW NBI and 20 MW ICRH) was simulated at two different levels of gas puff:  $0.5 \cdot 10^{22} \text{ s}^{-1}$  and  $1.0 \cdot 10^{22} \text{ s}^{-1}$ . Above this level of fuelling the simulations show a collapse of the temperature at the divertor target and the onset of a numerical instability in the code. This is an indication that the plasma is becoming detached and a thermal instability similar to a MARFE could be triggered in a similar real plasma discharge. This is not surprising given that, for this relatively low plasma current, the fusion power and the power flux across the separatrix are too low to sustain an attached divertor. A summary of the results is given in table 1 where we show the main steady-state plasma parameters achievable under these fuelling rates and heating conditions. The core and SOL electron density and electron and ion temperature profiles for the two cases are shown in figures 1 and 2, whereas the electron density, electron and ion temperature and the power density profiles on the outer and inner divertor target are shown in figures 3 and 4, respectively. It is worth noting that, despite the limits on fuelling rate, the average density remains above the threshold for neutral beam shine-through loads on the first wall ( $\sim 2.5\text{--}3.0 \cdot 10^{19} \text{ m}^{-3}$  [28]), which ensures that the full NBI power of 33 MW and ion energy of 1 MeV can be used in ITER for these plasma conditions.

### 4. Results at 7.5 MA

For the H-mode plasmas at 7.5 MA we performed five series of simulations: a fuelling rate scan at 5.3 T and 53 MW of additional power, a similar scan at 2.65 T and 53 MW of additional power, a third and fourth fuelling rate scans at 2.65 T and additional power reduced to 33 MW with both Be and W divertor and, finally, a fifth series of simulations at 2.65 T and 33 MW of additional power where gas fuelling was complemented with pellet injection.

**Table 1.** Summary of results from section 3. Main plasma parameters achievable for different fuelling and heating conditions in an ITER D-T H-mode plasma at 5 MA/5.3 T. (Be divertor).

$P_{\text{NBI}}$ ,  $P_{\text{ECRH}}$  and  $P_{\text{ICRH}}$  are the total NBI, ECRH and ICRH power respectively;  $\Gamma_{\text{D-T}}$  and  $\Gamma_{\text{Ne}}$  are the nominal main gas and Ne seeding throughput respectively;  $f_{\text{G}}$  is the Greenwald fraction;  $H_{98}$  is the improved confinement factor with respect to the ITERH-98P(y,2) scaling law;  $n_{\text{e}}(0)$  and  $\langle n_{\text{e}} \rangle$ ,  $T_{\text{e}}(0)$  and  $\langle T_{\text{e}} \rangle$ ,  $T_{\text{i}}(0)$  and  $\langle T_{\text{i}} \rangle$  are the on-axis and volume-average electron density and electron and ion temperature respectively;  $n_{\text{e,sep}}$  is the density at the separatrix;  $P_{\text{fus}}$  and  $Q$  are the fusion power and the fusion gain respectively,  $Z_{\text{eff}}$  is the effective charge;  $P_{\text{IT}}$  and  $P_{\text{OT}}$  are the peak power density on the inner and outer divertor target respectively;  $P_{\text{sep}}$ ,  $P_{\text{rad,core}}$  and  $P_{\text{rad,div}}$  are the power through the separatrix, radiated in the plasma core and in the divertor respectively. The same notation is used in all the tables in this paper.

Case	A	B
$P_{\text{NBI}}/P_{\text{ECRH}}/P_{\text{ICRH}}$ (MW)	33/-/20	33/-/20
$\Gamma_{\text{D-T}}$ ( $10^{22} \text{ s}^{-1}$ )/ $\Gamma_{\text{Ne}}$ ( $10^{20} \text{ s}^{-1}$ )	0.5/-	1.0/-
$f_{\text{G}}$	0.68	0.80
$H_{98}$	0.86	0.83
$n_{\text{e}}(0)/\langle n_{\text{e}} \rangle/n_{\text{e,sep}}$ ( $10^{19} \text{ m}^{-3}$ )	3.3/2.6/2.2	3.9/3.2/2.9
$T_{\text{e}}(0)/\langle T_{\text{e}} \rangle$ (keV)	13.0/5.4	11.4/4.4
$T_{\text{i}}(0)/\langle T_{\text{i}} \rangle$ (keV)	15.8/5.5	12.0/4.2
$P_{\text{fus}}$ (MW)/ $Q$	15.3/0.29	17.9/0.34
Divertor material	Be	Be
$Z_{\text{eff}}$	2.0	1.3
$P_{\text{IT}}/P_{\text{OT}}$ ( $\text{MW m}^{-2}$ )	1.6/2.8	0.9/1.4
$P_{\text{sep}}/P_{\text{rad,core}}/P_{\text{rad,div}}$ (MW)	42.2/0.5/13.2	48.7/0.5/10.7

#### 4.1. Results at 7.5 MA/5.3 T/53 MW and 7.5 MA/2.65 T/53 MW

The results of the simulations at 7.5 MA and 53 MW of additional heating power are summarized in tables 2 and 3 and show that, for fuelling rates up to  $1.0 \cdot 10^{22} \text{ s}^{-1}$ , at 5.3 T one can reach a higher core temperature than at 2.65 T, because of a reduced sawtooth activity and a higher density for the same fuelling rate, due to a higher separatrix density. However, because the SOL heat flux width is larger at 5.3 T than at 2.65 T (due to the longer connection length), this leads to lower SOL power densities and an earlier onset of detachment at lower fuelling rates for 5.3 T than for 2.65 T. As a consequence, higher plasma densities are reached at 2.65 T at higher fuelling rates (up to  $2.0 \cdot 10^{22} \text{ s}^{-1}$ ). This can be seen from figure 5, where we show the electron density and electron and ion temperature profiles in the SOL for two simulations with  $\Gamma_{\text{D-T}} = 1.0 \cdot 10^{22} \text{ s}^{-1}$  at 5.3 T and 2.65 T. In figures 6 and 7 we show, for the same two simulations, the electron density, electron and ion temperature and power density profiles on the outer and inner divertor target, respectively.

#### 4.2. Results at 7.5MA/2.65T/33 MW. Be and W divertor

The results obtained for a reduction in auxiliary power to 33 MW are summarized in tables 4 (Be divertor) and 5 (W divertor) and are comparable to those with 53 MW. It is worth emphasizing that, in the case of W divertor, there are no impurities in the plasmas because we do not consider W sputtering, as it appears from the values of  $Z_{\text{eff}} \approx 1$ . In these simulations, the ratio between the net power flowing through the separatrix

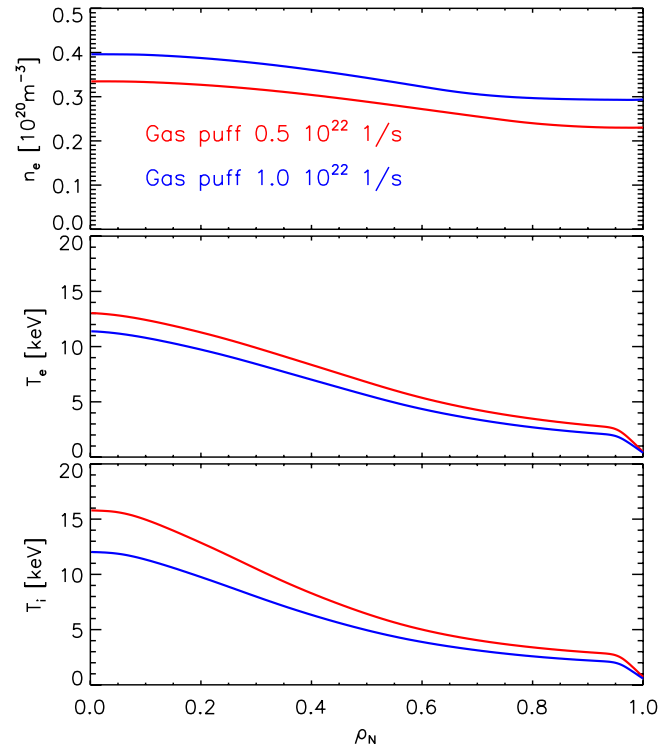


**Figure 1.** Core plasma electron density and electron and ion temperature profiles for case A (red) and B (blue) in table 1.  $I_{\text{p}} = 5 \text{ MA}$ ,  $B_{\text{T}} = 5.3 \text{ T}$ ,  $P_{\text{aux}} = 53 \text{ MW}$ .

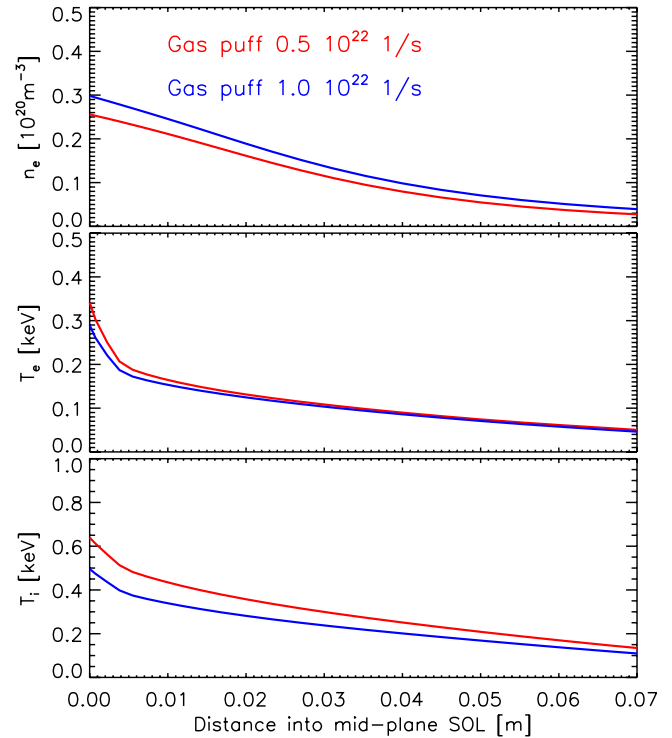


**Figure 2.** Mid-plane SOL electron density and electron and ion temperature profiles for case A (red) and B (blue) in table 1.  $I_{\text{p}} = 5 \text{ MA}$ ,  $B_{\text{T}} = 5.3 \text{ T}$ ,  $P_{\text{aux}} = 53 \text{ MW}$ .

and the L-H transition power threshold,  $P_{\text{net}}/P_{\text{L-H}}$  is between 1.5 and 2.0, but the plasma remains deeply in H-mode. Core temperatures and densities are reduced by about 2 keV and  $0.25 \cdot 10^{19} \text{ m}^{-3}$ , due to the lower power input. The maximum

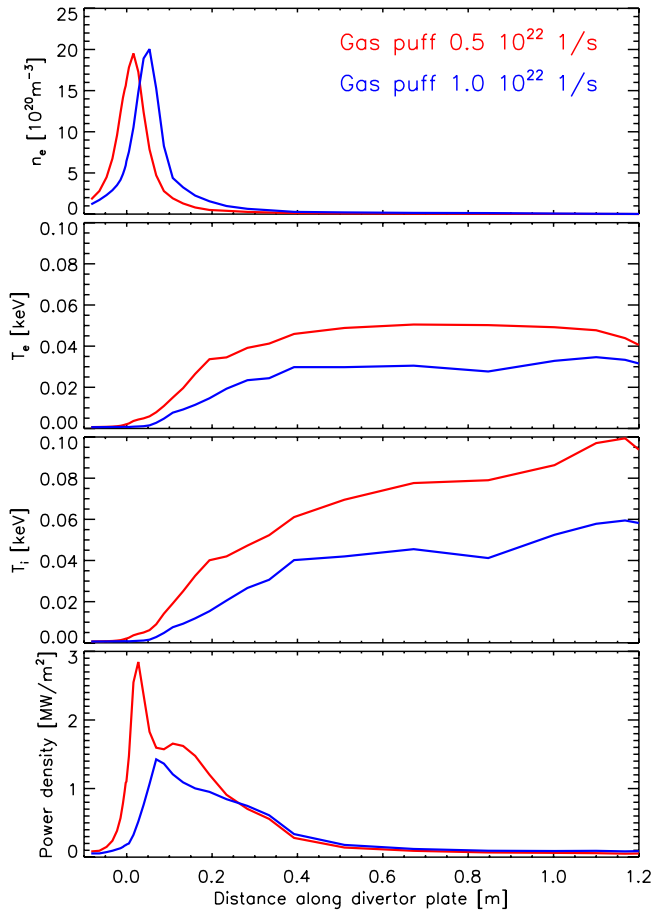


**Figure 3.** Outer divertor target electron density, electron and ion temperature and power density profiles for case A (red) and B (blue) in table 1.  $I_p = 5$  MA,  $B_T = 5.3$  T,  $P_{aux} = 53$  MW.

gas puff rates allowed before the appearance of numerical problems indicating the occurrence of a thermal instability in the divertor is of the same order of magnitude as for the case with 53 MW of additional power. The plasma volume-average density tends to saturate for  $\Gamma_{D-T} \approx 2.0 \cdot 10^{22} \text{ s}^{-1}$ . For higher gas puff rates, the onset of a numerical instability in the simulations indicates that the plasma starts to become detached. For low gas puff rates ( $\Gamma_{D-T} \leq 1.0 \cdot 10^{22} \text{ s}^{-1}$ ), the ion temperature on the outer target is predicted to exceed the critical level for W sputtering by light impurities of  $\sim 5$  eV [29] in regions with significant ion current density. Although core temperatures in the order of  $\sim 10$  keV can be obtained due to operation at low density, the fusion power remains  $\sim 22$  MW, giving  $Q$  slightly below 0.7. The power flux across the separatrix  $P_{sep}$  thus remains close to  $P_{aux}$ . Due to the low  $P_{sep}$ , the power density on the targets can be maintained well below  $10 \text{ MW m}^{-2}$  without the need for Ne seeding, even for low gas fuelling rates. In cases with Be targets,  $Z_{eff}$  is only marginally higher than in the cases with W targets. This seems to be due to operation at low power where Be sputtering at the target plates is much lower compared to the baseline scenario scans with Be targets at higher power, which will be presented in section 6.1.  $Z_{eff}$  is also significantly lower compared to the same gas puff scan at 53 MW. This may explain why predicted edge densities do not deviate considerably for the cases with  $P_{aux} = 33$  MW

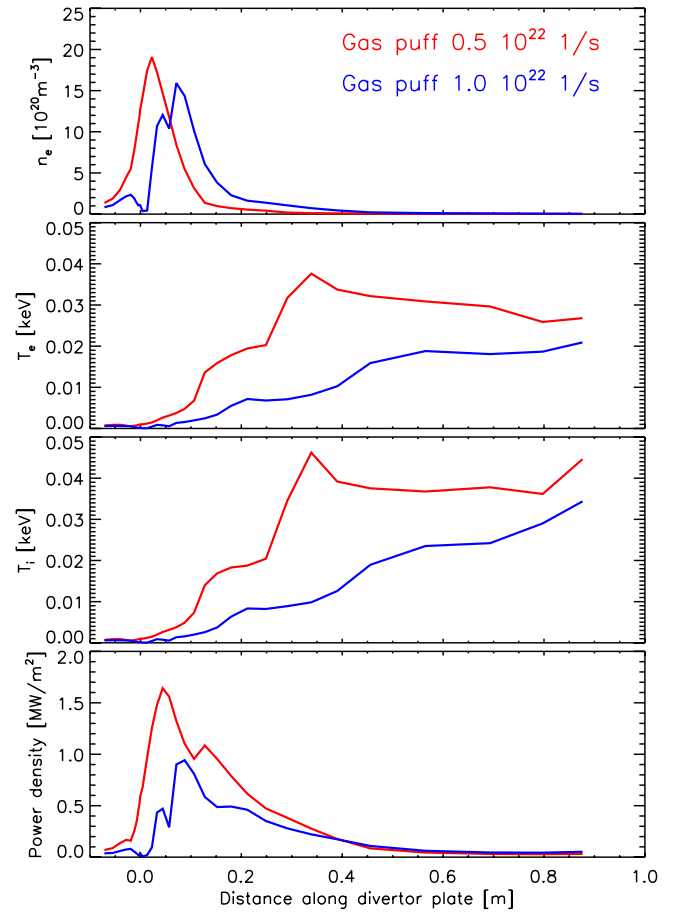


**Figure 4.** Inner divertor target electron density, electron and ion temperature and power density profiles for case A (red) and B (blue) in table 1.  $I_p = 5$  MA,  $B_T = 5.3$  T,  $P_{aux} = 53$  MW.

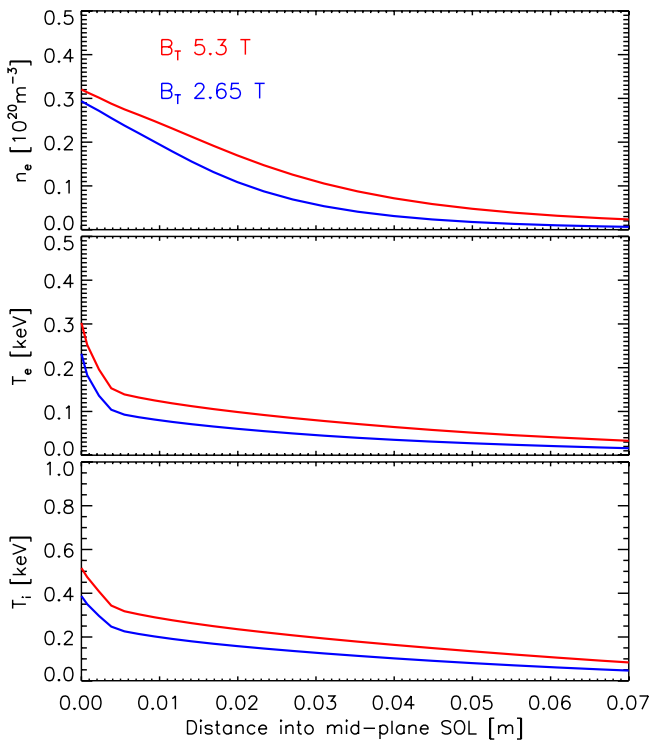
**Table 2.** Summary of results from section 4.1 ( $B_T = 5.3$  T). Main plasma parameters achievable for different fuelling and heating conditions in an ITER D-T H-mode plasma at 7.5 MA/5.3 T and 53 MW of additional power.

Case	A	B
$P_{NBI}/P_{ECRH}/P_{ICRH}$ (MW)	33/-/20	33/-/20
$\Gamma_{D-T}$ ( $10^{22} \text{ s}^{-1}$ )/ $\Gamma_{Ne}$ ( $10^{20} \text{ s}^{-1}$ )	0.5/-	1.0/-
$f_G$	0.58	0.65
$H_{98}$	0.94	0.92
$n_e(0)/\langle n_e \rangle/n_{e,sep}$ ( $10^{19} \text{ m}^{-3}$ )	4.3/3.4/2.7	4.8/3.8/3.1
$T_e(0)/\langle T_e \rangle$ (keV)	15.2/7.2	14.3/6.6
$T_i(0)/\langle T_i \rangle$ (keV)	18.0/7.3	16.0/6.5
$P_{fus}$ (MW)/ $Q$	47.0/0.89	51.3/0.97
Divertor material	Be	Be
$Z_{eff}$	1.6	1.4
$P_{IT}/P_{OT}$ ( $\text{MW m}^{-2}$ )	2.0/3.7	1.5/2.4
$P_{sep}/P_{rad,core}/P_{rad,div}$ (MW)	54.0/0.4/13.2	53.2/0.5/11.7

and  $P_{aux} = 53$  MW. Higher  $P_{sep}$  in case with  $P_{aux} = 53$  MW seems to be partially compensated by increased impurity radiation in the SOL. Due to the small difference in impurity contamination, the results obtained with Be targets are quite similar to those obtained with W targets. Switching from Be to W targets, the core density is increased by a few percent only, whereas power densities and temperatures on the target plates

**Table 3.** Summary of results from section 4.1 ( $B_T = 2.65$  T). Main plasma parameters achievable for different fuelling and heating conditions in an ITER D-T H-mode plasma at 7.5 MA/2.65 T and 53 MW of additional power.

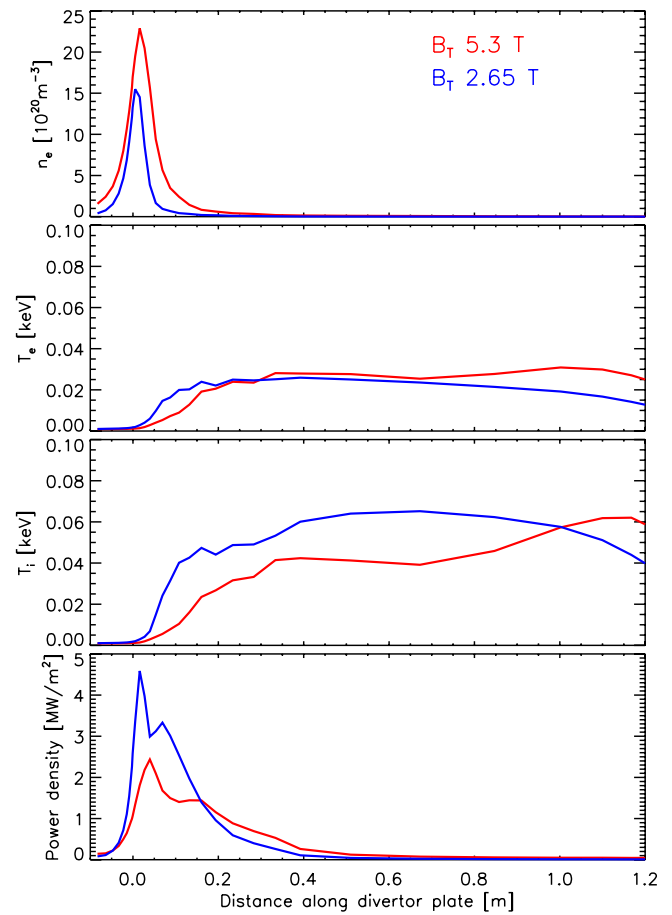
Case	A	B	C	D
$P_{\text{NBI}}/P_{\text{ECRH}}/P_{\text{ICRH}}$ (MW)	33/-/20	33/-/20	33/-/20	33/-/20
$\Gamma_{\text{D-T}} (10^{22} \text{ s}^{-1})/\Gamma_{\text{Ne}} (10^{20} \text{ s}^{-1})$	0.5/-	1.0/-	1.5/-	2.0/-
$f_G$	0.48	0.60	0.66	0.68
$H_{98}$	0.99	0.96	0.95	0.95
$n_e(0)/\langle n_e \rangle/n_{e,\text{sep}} (10^{19} \text{ m}^{-3})$	3.4/2.8/2.2	4.4/3.5/2.8	4.8/3.9/3.1	5.0/4.0/3.3
$T_e(0)/\langle T_e \rangle$ (keV)	13.0/7.6	11.5/6.4	10.8/5.9	10.5/5.7
$T_i(0)/\langle T_i \rangle$ (keV)	16.0/8.0	12.8/6.4	11.7/5.8	11.3/5.6
$P_{\text{fus}} (\text{MW})/Q$	34.9/0.66	38.5/0.73	39.3/0.74	39.8/0.75
Divertor material	Be	Be	Be	Be
$Z_{\text{eff}}$	1.6	1.4	1.3	1.3
$P_{\text{IT}}/P_{\text{OT}} (\text{MW m}^{-2})$	3.9/6.1	2.9/4.6	2.5/3.3	2.6/2.7
$P_{\text{sep}}/P_{\text{rad,core}}/P_{\text{rad,div}} (\text{MW})$	49.1/0.2/9.8	49.5/0.5/8.3	49.2/0.5/7.4	50.9/0.6/6.9

**Figure 5.** Mid-plane SOL electron density and electron and ion temperature profiles for case B in table 2 (red,  $I_p = 7.5$  MA,  $B_T = 5.3$  T,  $P_{\text{aux}} = 53$  MW) and case B in table 3 (blue,  $I_p = 7.5$  MA,  $B_T = 2.65$  T,  $P_{\text{aux}} = 53$  MW).

are slightly increased as a consequence of reduced impurity radiation in the SOL, because, as said above, in our modelling no impurities are produced at the divertor for the W target.

#### 4.3. Results at 75MA/2.65T/33 MW. Discrete pellets

To study the use of pellet fuelling on this ITER scenario, we started from a simulation of a 7.5 MA, 2.65 T plasma with 33 MW of additional heating power and  $5.0 \cdot 10^{21} \text{ s}^{-1}$  D-T gas puff from the main chamber wall, which reached a steady-state volume-average density of  $3.4 \cdot 10^{19} \text{ m}^{-3}$ . This simulation is similar to the one in the first column of table 4 except for the addition of a  $1.0 \cdot 10^{20} \text{ s}^{-1}$  Ne gas puff from the divertor

**Figure 6.** Outer divertor target electron density, electron and ion temperature and power density profiles for case B in table 2 (red,  $I_p = 7.5$  MA,  $B_T = 5.3$  T,  $P_{\text{aux}} = 53$  MW) and case B in table 3 (blue,  $I_p = 7.5$  MA,  $B_T = 2.65$  T,  $P_{\text{aux}} = 53$  MW).

region. The reference simulation was continued for 2 s by introducing discrete pellets (mass  $4.4 \cdot 10^{21}$  atoms, speed  $300 \text{ m s}^{-1}$ , composition 50–50 D-T) and prescribing a target volume-average density for the feed-back mechanism controlling the pellet injection of  $4 \cdot 10^{19} \text{ m}^{-3}$  and  $5 \cdot 10^{19} \text{ m}^{-3}$ . The choice for these target volume-average densities was dictated by the fact that we wanted, on one side, to increase the

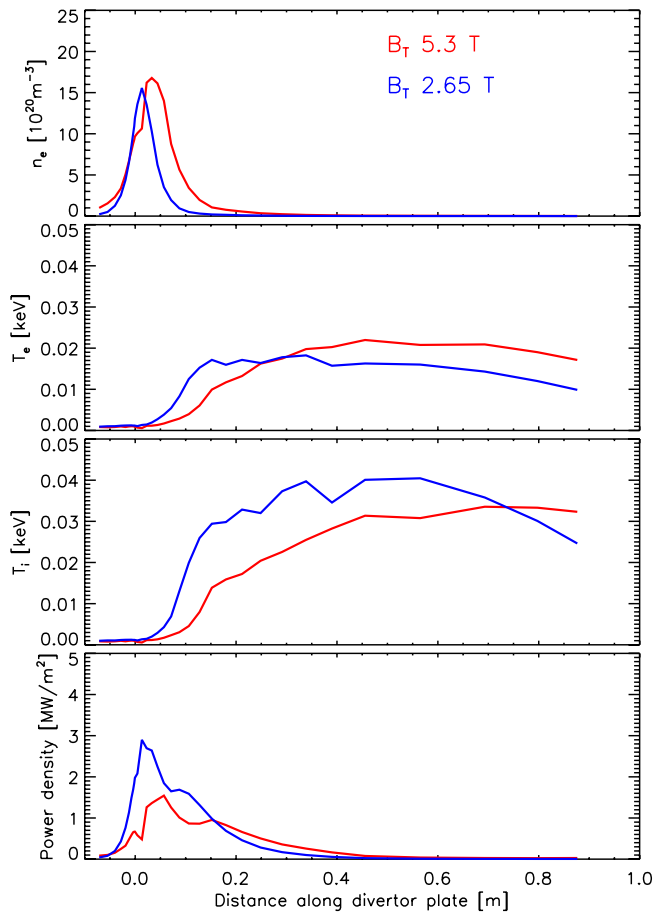


**Figure 7.** Inner divertor target electron density, electron and ion temperature and power density profiles for case B in table 2 (red,  $I_p = 7.5$  MA,  $B_T = 5.3$  T,  $P_{aux} = 53$  MW) and case B in table 3 (blue,  $I_p = 7.5$  MA,  $B_T = 2.65$  T,  $P_{aux} = 53$  MW).

Greenwald fraction from the reference case to a value equivalent to the 15 MA, 5.3 T plasma (i.e.  $f_G \approx 0.85$ ) and, on the other side, to test an intermediate value between the reference case and the highest Greenwald fraction prescribed.

The background gas puff was maintained at  $5.0 \cdot 10^{21} \text{ s}^{-1}$ . For the scenario with target volume-average density  $4 \cdot 10^{19} \text{ m}^{-3}$  a case was run with background gas puff at  $1.0 \cdot 10^{21} \text{ s}^{-1}$  to test the effect on the divertor power load. The results are illustrated in figure 8, which shows that the target volume-average densities are easily achieved with the injection of five pellets in the case of  $5 \cdot 10^{19} \text{ m}^{-3}$  target density and maintained with a pellet injection frequency of  $\sim 2$  Hz, whereas only two pellets are required to achieve the target density of  $4 \cdot 10^{19} \text{ m}^{-3}$  and a pellet frequency of  $\sim 1$  Hz is required to maintain it.

As for the power density on the divertor plates, even in the least favourable case (namely target density  $4 \cdot 10^{19} \text{ m}^{-3}$  and background gas puff  $1.0 \cdot 10^{21} \text{ s}^{-1}$ ) it did not exceed  $2 \text{ MW m}^{-2}$  on the inner target and  $3 \text{ MW m}^{-2}$  on the outer target. It should be noted that the main effect on the core plasma of the reduction in background gas puff from  $5.0 \cdot 10^{21} \text{ s}^{-1}$  to  $1.0 \cdot 10^{21} \text{ s}^{-1}$  is a modest increase in the speed of the density decay after pellet injection, which could imply a slightly higher pellet frequency required to maintain the target volume-average density.

The reaction of the divertor to the train of pellets injected to rise the density to  $5 \cdot 10^{19} \text{ m}^{-3}$  is illustrated in figure 9, where we show the evolution of the volume-average electron density in the core plasma and the electron density and temperature at the inner and outer divertor target. It can be seen that both divertor targets experience a drop in electron density and temperature in correspondence of the pellet induced density ramp (this is particularly true for the outer divertor), indicating that the divertor is approaching detachment.

## 5. Results at 10 MA

For plasma current levels of 10 MA and above the picture of the density behaviour changes because the fusion power and the reduction of the transport in the ETB start to play a role. The heat flux through the separatrix is increased by  $\sim 20$ – $25$  MW due to alpha heating. This allows the achievement of a higher density at the separatrix by gas fuelling before the onset of detachment, which in turn allows for higher plasma densities in the core to be achievable by gas fuelling. The simulation results indicate that, in purely gas fuelled plasmas for  $I_p \geq 10$  MA without Ne seeding, it may be difficult to maintain the ion temperature below the guideline value for W sputtering by light impurities of  $\sim 5 \text{ eV}$  on the outer target near the strike point location, where the ion current density peaks. For this scenario, we carried out four series of runs. The first is a simple scan of the gas fuelling rate without pellet injection or Ne seeding, the second is a density scan obtained by varying the injection frequency of discrete pellets in presence of some Ne seeding, the third is a scan in the Ne seeding rate and the fourth is a study to analyze the sensitivity of the results to the width of the ETB.

### 5.1. Results 10 MA/5.3 T/53 MW

The results of the scan of the gas fuelling rate are summarized in table 6. It can be seen that for this particular heating and fuelling scheme  $f_G \leq 0.7$  and  $Q \approx 2$ . Because of the relatively modest fusion power generated in this scenario and the divertor radiation provided by Be, the power density on the divertor plate remains below  $10 \text{ MW m}^{-2}$ .

### 5.2. Results at 10 MA/5.3 T/53 MW. Discrete pellets

The use of discrete pellets was analysed also in the case of a 10 MA, 5.3 T ITER D-T H-mode case with 33 MW of NB and 20 MW of ICRH, background D-T gas puff  $1.0 \cdot 10^{22} \text{ s}^{-1}$  from the main chamber and  $1.0 \cdot 10^{20} \text{ s}^{-1}$  Ne gas puff from the divertor region, which reached a steady-state volume-average density of  $3.9 \cdot 10^{19} \text{ m}^{-3}$ .

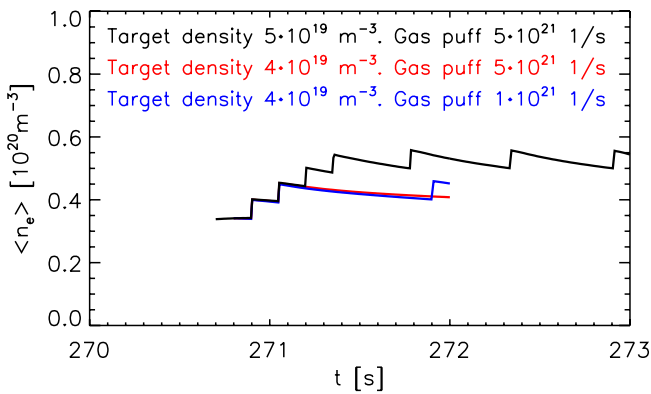
The reference simulation was continued for 1 s by adding discrete pellets (mass  $4.4 \cdot 10^{21}$  atoms, speed  $300 \text{ m s}^{-1}$ , composition 50–50 D-T), requested by a feed-back mechanism that injected a pellet whenever the plasma volume-average density dropped below a prescribed level. The requested volume-average target densities were  $4.5 \cdot 10^{19} \text{ m}^{-3}$  and  $6.6 \cdot 10^{19} \text{ m}^{-3}$ . As for the simulations at 7.5 MA and 5.3 T, the higher level

**Table 4.** Summary of results from section 4.2 (Be divertor). Main plasma parameters achievable for different fuelling and heating conditions in an ITER D-T H-mode plasma at 7.5 MA/2.65 T and 33 MW of additional power.

Case	A	B	C	D
$P_{\text{NBI}}/P_{\text{ECRH}}/P_{\text{ICRH}}$ (MW)	33/–/–	33/–/–	33/–/–	33/–/–
$\Gamma_{\text{D-T}} (10^{22} \text{ s}^{-1})/\Gamma_{\text{Ne}} (10^{20} \text{ s}^{-1})$	0.5/–	1.0/–	1.5/–	2.0/–
$f_{\text{G}}$	0.43	0.55	0.60	0.65
$H_{98}$	1.00	0.97	0.96	0.95
$n_{\text{e}}(0)/\langle n_{\text{e}} \rangle/n_{\text{e,sep}} (10^{19} \text{ m}^{-3})$	3.3/2.6/2.0	4.0/3.2/2.5	4.4/3.5/2.8	4.7/3.8/3.1
$T_{\text{e}}(0)/\langle T_{\text{e}} \rangle$ (keV)	11.1/7.0	9.7/5.9	9.3/5.5	8.9/5.2
$T_{\text{i}}(0)/\langle T_{\text{i}} \rangle$ (keV)	9.8/6.2	8.6/5.3	8.2/5.0	7.8/4.7
$P_{\text{fus}} (\text{MW})/Q$	21.6/0.65	22.3/0.68	22.2/0.67	22.2/0.67
Divertor material	Be	Be	Be	Be
$Z_{\text{eff}}$	1.14	1.06	1.05	1.05
$P_{\text{IT}}/P_{\text{OT}} (\text{MW m}^{-2})$	2.3/3.8	1.8/2.0	1.5/1.7	1.6/1.1
$P_{\text{sep}}/P_{\text{rad,core}}/P_{\text{rad,div}} (\text{MW})$	48.1/0.06/4.0	40.5/0.04/2.2	42.5/0.07/1.9	42.7/0.07/1.8

**Table 5.** Summary of results from section 4.2 (W divertor). Main plasma parameters achievable for different fuelling and heating conditions in an ITER D-T H-mode plasma at 7.5 MA/2.65 T and 33 MW of additional power.

Case	A	B	C	D
$P_{\text{NBI}}/P_{\text{ECRH}}/P_{\text{ICRH}}$ (MW)	33/–/–	33/–/–	33/–/–	33/–/–
$\Gamma_{\text{D-T}} (10^{22} \text{ s}^{-1})/\Gamma_{\text{Ne}} (10^{20} \text{ s}^{-1})$	0.5/–	1.0/–	1.5/–	2.0/–
$f_{\text{G}}$	0.43	0.56	0.63	0.67
$H_{98}$	1.02	0.97	0.95	0.95
$n_{\text{e}}(0)/\langle n_{\text{e}} \rangle/n_{\text{e,sep}} (10^{19} \text{ m}^{-3})$	3.2/2.5/1.8	4.2/3.3/2.6	4.6/3.7/2.9	4.9/3.9/3.1
$T_{\text{e}}(0)/\langle T_{\text{e}} \rangle$ (keV)	11.0/7.0	9.5/5.7	8.7/5.3	8.5/5.0
$T_{\text{i}}(0)/\langle T_{\text{i}} \rangle$ (keV)	9.7/6.1	8.3/5.1	7.9/4.8	7.7/4.6
$P_{\text{fus}} (\text{MW})/Q$	22.4/0.68	22.7/0.69	22.5/0.68	22.4/0.68
Divertor material	W	W	W	W
$Z_{\text{eff}}$	1.00	1.00	1.00	1.02
$P_{\text{IT}}/P_{\text{OT}} (\text{MW m}^{-2})$	2.3/6.7	1.8/2.6	1.6/1.9	1.7/1.2
$P_{\text{sep}}/P_{\text{rad,core}}/P_{\text{rad,div}} (\text{MW})$	45.4/<0.01/<0.01	47.3/0.01/<0.01	47.6/0.04/0.01	47.0/0.15/0.7

**Figure 8.** Evolution and control of the plasma volume-average density by means of pellet injection in 7.5 MA/2.65 T ITER D-T H-mode with 33 MW of NB for different target volume-average densities and with different levels of back-ground gas puff. The target densities are easily achieved and maintained.

represents a Greenwald fraction equivalent to a volume-average density of  $1.0 \cdot 10^{20} \text{ m}^{-3}$  at 15 MA, whereas the lower one is an intermediate value between the reference case and the highest density required. For each target volume-average density, we prescribed two levels of background gas puff, namely  $7.5 \cdot 10^{21} \text{ s}^{-1}$  and  $1.0 \cdot 10^{21} \text{ s}^{-1}$ , to analyse the impact on the

power load on the divertor. The results in figure 10 show that, in the case of target volume-average density  $6.6 \cdot 10^{19} \text{ m}^{-3}$ , seven pellets are requested at the maximum allowed frequency, but, shortly before reaching the target value, the particle throughput imposed on the plasma by such a high fuelling rate causes the last injected pellets to overload the SOL with gas, forcing the detachment of the divertor and the numerical collapse of the simulation. This is shown in figure 11, where we plot the volume-average electron density in the plasma core and electron density and temperature at the inner and outer divertor target. The continuous decrease of the temperature at the outer divertor corresponding to the density ramp-up and leading to the numerical collapse of the simulation triggered by the last pellet can be clearly seen. The situation could be improved by increasing the duration of the minimum interval between consecutive pellets, by reducing the pellet mass or by reducing even more the back-ground gas-puff. This result shows that the optimization of the fuelling by pellets together with sustainment of partially attached detachment divertor plasma conditions is a complex issue which requires the careful adjustment of gas fuelling, impurity seeding and pellet injection parameters (size and frequency).

For the case with target volume-average density  $4.5 \cdot 10^{19} \text{ m}^{-3}$ , it can be seen that two pellets are needed to

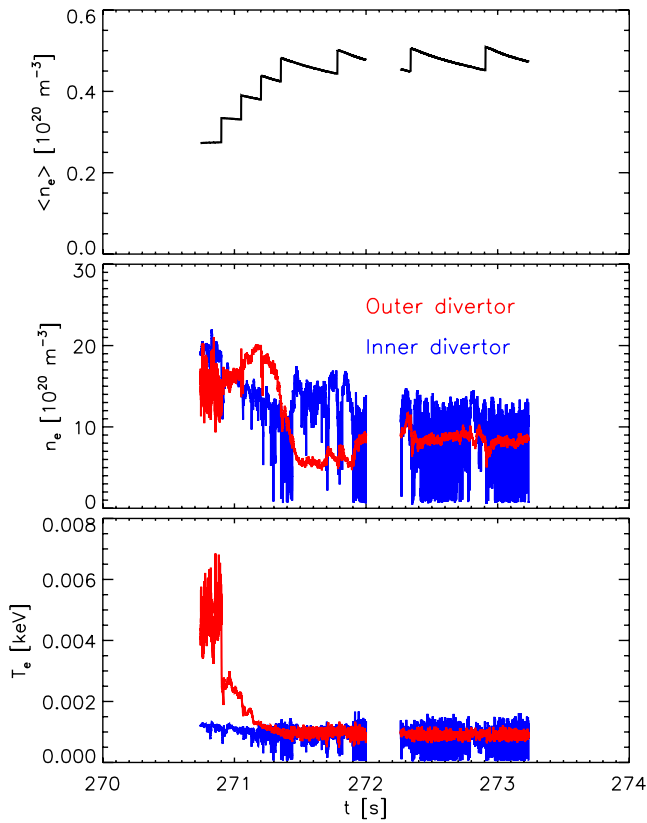


**Figure 9.** Time evolution of the volume-average electron density in the core plasma and the electron density and temperature at the intersection of the separatrix with the outer (red) and inner (blue) divertor target in a 7.5 MA/2.65 T ITER D-T H-mode with 33 MW of NB and pellets injected to achieve a volume-average core plasma electron density of  $5 \cdot 10^{19} \text{ m}^{-3}$ .

**Table 6.** Summary of results from section 5.1. Main plasma parameters achievable for different fuelling and heating conditions in an ITER D-T H-mode plasma at 10 MA/5.3 T and 53 MW of additional power.

Case	A	B	C
$P_{\text{NBI}}/P_{\text{ECRH}}/P_{\text{ICRH}}$ (MW)	33/-/20	33/-/20	33/-/20
$\Gamma_{\text{D-T}} (10^{22} \text{ s}^{-1})/\Gamma_{\text{Ne}} (10^{20} \text{ s}^{-1})$	0.75/-	1.25/-	2.0/-
$f_{\text{G}}$	0.5	0.6	0.7
$H_{98}$	0.94	0.91	0.89
$n_e(0)/\langle n_e \rangle/n_{e,\text{sep}}$ ( $10^{19} \text{ m}^{-3}$ )	4.9/3.9/3.1	5.8/4.6/3.8	6.7/5.4/4.5
$T_e(0)/\langle T_e \rangle$ (keV)	17.1/8.9	15.7/7.7	14.4/6.8
$T_i(0)/\langle T_i \rangle$ (keV)	19.6/9.0	16.8/7.6	14.9/6.7
$P_{\text{fus}} (\text{MW})/Q$	99.1/1.87	108.2/2.04	113.2/2.14
Divertor material	Be	Be	Be
$Z_{\text{eff}}$	1.4	1.2	1.1
$P_{\text{IT}}/P_{\text{OT}}$ ( $\text{MW m}^{-2}$ )	3.3/7.5	2.9/6.5	2.6/3.4
$P_{\text{sep}}/P_{\text{rad,core}}/P_{\text{rad,div}}$ (MW)	68.1/0.7/16.6	68.3/0.5/8.9	68.4/0.5/8.6

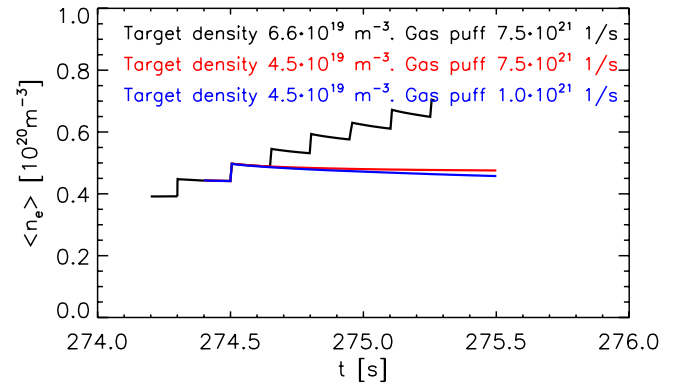


**Figure 10.** Evolution and control of the plasma volume-average density by means of pellet injection in 10 MA/5.3 T ITER D-T H-mode with 33 MW of NB and 20 MW of ICRH for different target volume-average densities and with different levels of background gas puff. The target densities are easily achieved and maintained.

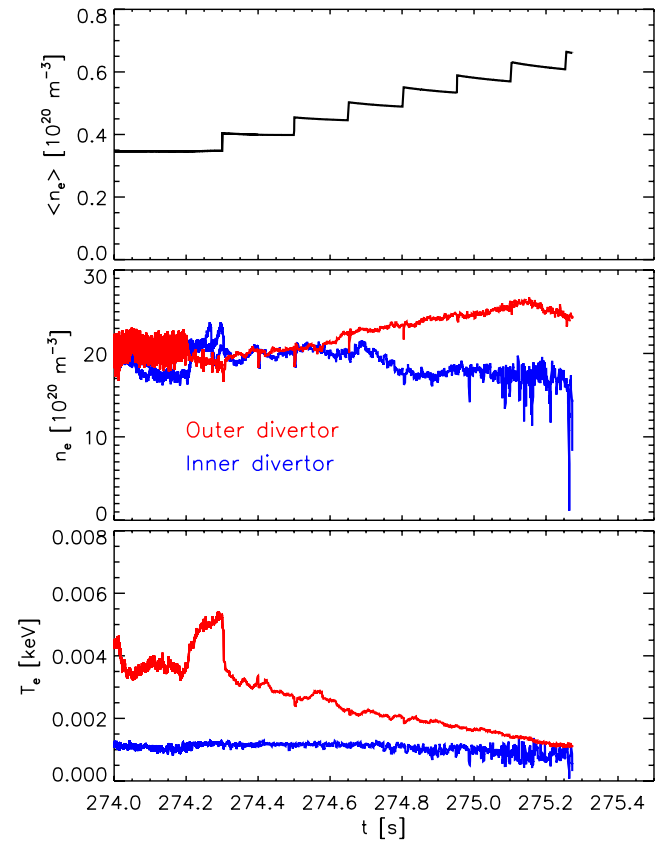


**Figure 11.** Time evolution of the volume-average electron density in the core plasma and the electron density and temperature at the intersection of the separatrix with the outer (red) and inner (blue) divertor target in a 10 MA/5.3 T ITER D-T H-mode with 33 MW of NB and 20 MW of ICRH and pellets injected to achieve a volume-average core plasma electron density of  $6.6 \cdot 10^{19} \text{ m}^{-3}$ .

reach the reference value (figure 10, red curve). Once the requested volume-average density is reached a level of background gas puff of  $7.5 \cdot 10^{21} \text{ s}^{-1}$  is almost sufficient to fuel the plasma without the need of any further pellet injection,

**Table 7.** Summary of results from section 5.3 (Ne seeding). Main plasma parameters achievable for different fuelling and heating conditions in an ITER D-T H-mode plasma at 10 MA/5.3 T and 53 MW of additional power.

Case	A	B	C
$P_{\text{NBI}}/P_{\text{ECRH}}/P_{\text{ICRH}}$ (MW)	33/-/20	33/-/20	33/-/20
$\Gamma_{\text{D-T}} (10^{22} \text{ s}^{-1})/\Gamma_{\text{Ne}} (10^{20} \text{ s}^{-1})$	0.5/2.0	0.5/3.0	1.0/3.0
$f_{\text{G}}$	0.47	0.46	0.46
$H_{98}$	0.98	0.98	0.97
$n_{\text{e}}(0)/\langle n_{\text{e}} \rangle/n_{\text{e,sep}} (10^{19} \text{ m}^{-3})$	5.0/3.7/2.7	4.9/3.7/2.7	4.9/3.6/2.7
$T_{\text{e}}(0)/\langle T_{\text{e}} \rangle$ (keV)	17.5/9.5	17.8/9.6	17.8/9.6
$T_{\text{i}}(0)/\langle T_{\text{i}} \rangle$ (keV)	20.4/9.7	20.8/10.0	21.0/9.9
$P_{\text{fus}} \text{ (MW)}/Q$	105.2/1.98	104.4/1.97	103.1/1.95
Divertor material	Be	Be	Be
$Z_{\text{eff}}$	1.6	1.7	1.7
$P_{\text{IT}}/P_{\text{OT}} \text{ (MW m}^{-2}\text{)}$	2.7/8.5	2.5/8.0	2.5/7.5
$P_{\text{sep}}/P_{\text{rad,core}}/P_{\text{rad,div}} \text{ (MW)}$	63.1/1.1/19.9	64.6/1.3/21.9	65.6/1.4/22.2

**Table 8.** Summary of results from section 5.4 (sensitivity to ETB width). Main plasma parameters achievable for different ETB and current profile assumptions in an ITER D-T H-mode plasma at 10 MA/5.3 T and 53 MW of additional power.  $\rho_{\text{ETB}}$  is the position of the top of the ETB in terms of normalized toroidal flux and  $l_{\text{i}}(3)$  is the plasma internal inductance.

Case	A	B	C	D
$P_{\text{NBI}}/P_{\text{ECRH}}/P_{\text{ICRH}}$ (MW)	33/20/-	33/20/-	33/20/-	33/20/-
$\Gamma_{\text{D-T}} (10^{22} \text{ s}^{-1})/\Gamma_{\text{Ne}} (10^{20} \text{ s}^{-1})$	1.5/-	1.5/-	1.5/-	1.5/-
$f_{\text{G}}$	0.48	0.48	0.48	0.50
$H_{98}$	1.10	1.00	0.89	0.58
$n_{\text{e}}(0)/\langle n_{\text{e}} \rangle/n_{\text{e,sep}} (10^{19} \text{ m}^{-3})$	4.8/3.8/3.3	4.9/3.8/3.3	4.9/3.8/3.1	4.8/3.9/3.3
$T_{\text{e}}(0)/\langle T_{\text{e}} \rangle$ (keV)	19.9/11.2	18.5/10.0	17.0/8.7	12.3/5.6
$T_{\text{i}}(0)/\langle T_{\text{i}} \rangle$ (keV)	15.9/9.4	14.4/8.3	13.0/7.2	8.4/4.4
$P_{\text{fus}} \text{ (MW)}/Q$	103.5/ 1.95	80.6/1.52	60.2/1.14	21.3/0.40
Divertor material	Be	Be	Be	Be
$Z_{\text{eff}}$	1.38	1.37	1.37	1.37
$\rho_{\text{ETB}}$	0.92	0.93	0.94	0.94
$l_{\text{i}}(3)$	0.68	0.68	0.68	0.50

whereas with a lower back-ground gas puff of  $1.0 \cdot 10^{21} \text{ s}^{-1}$  a pellet injection frequency of 1 Hz would be required to maintain the volume-average plasma density at the prescribed value.

As for the divertor, we can see that at a gas puff rate of  $7.5 \cdot 10^{21} \text{ s}^{-1}$  the power load remains below  $3 \text{ MW m}^{-2}$  on the inner target and below  $6 \text{ MW m}^{-2}$  on the outer target. Dropping the intensity of the gas puff to  $1.0 \cdot 10^{21}$  increases the power density on the inner target to  $7 \text{ MW m}^{-2}$  and on the outer target to just above  $10 \text{ MW m}^{-2}$ , indicating that such a low level of gas puff is marginal for the ITER divertor.

### 5.3. Results at 10 MA/5.3 T/53 MW. Impurity seeding

In an attempt to see if it was possible further reduce the power loads to  $\approx 5 \text{ MW m}^{-2}$  in a 10 MA, 5.3 T ITER D-T H-mode plasma, we carried out simulations with additional Ne seeding on top of the D-T fuelling. The levels of D-T fuelling and Ne seeding used in the simulations are shown in table 7. The results (also shown in table 7) indicate that, even if the Ne seeding rate is increased up to  $3.0 \cdot 10^{20} \text{ s}^{-1}$  (resulting in a Ne content of to  $1.3 \cdot 10^{21}$  particles and a rise

**Table 9.** Summary of results from section 5.4 (sensitivity to heating scheme). Main plasma parameters achievable for different NBI, ECRH and ICRH combinations in an ITER D-T H-mode plasma at 10 MA/5.3 T and 53 MW of additional power.

Case	A	B
$P_{\text{NBI}}/P_{\text{ECRH}}/P_{\text{ICRH}}$ (MW)	33/20/-	33/-/20
$\Gamma_{\text{D-T}} (10^{22} \text{ s}^{-1})/\Gamma_{\text{Ne}} (10^{20} \text{ s}^{-1})$	1.5/-	1.5/-
$f_{\text{G}}$	0.48	0.48
$H_{98}$	1.00	1.03
$n_{\text{e}}(0)/\langle n_{\text{e}} \rangle/n_{\text{e,sep}} (10^{19} \text{ m}^{-3})$	4.8/ 3.8/3.1	4.8/3.8/3.1
$T_{\text{e}}(0)/\langle T_{\text{e}} \rangle$ (keV)	18.5/10.0	18.2/ 9.7
$T_{\text{i}}(0)/\langle T_{\text{i}} \rangle$ (keV)	14.5/8.3	21.0/9.9
$P_{\text{fus}} \text{ (MW)}/Q$	80.6/ 1.52	120.4/2.27
Divertor material	Be	Be
$Z_{\text{eff}}$	1.37	1.37
$\rho_{\text{ETB}}$	0.93	0.93
$l_{\text{i}}(3)$	0.68	0.68

in Ne radiation up to 18 MW), the effect on the electron target temperatures and the total power densities at the targets are minimal. Throughout the simulation the peak power densities at the inner and outer targets remain at  $\sim 2.7 \text{ MW m}^{-2}$  and  $\sim 8.0 \text{ MW m}^{-2}$  respectively. Only when we increase the D-T

**Table 10.** Summary of results from section 6.1 (Be divertor). Main plasma parameters achievable for different fuelling and heating assumptions in an ITER D-T H-mode plasma at 15 MA/5.3 T and 53 MW of additional power.

Case	A	B	C
$P_{\text{NBI}}/P_{\text{ECRH}}/P_{\text{ICRH}}$ (MW)	33/-/20	33/-/20	33/-/20
$\Gamma_{\text{D-T}} (10^{22} \text{ s}^{-1})/\Gamma_{\text{Ne}} (10^{20} \text{ s}^{-1})$	1.0/-	2.0/-	3.0/-
$f_{\text{G}}$	0.48	0.52	0.58
$H_{98}$	0.94	0.93	0.92
$n_{\text{e}}(0)/\langle n_{\text{e}} \rangle/n_{\text{e,sep}} (10^{19} \text{ m}^{-3})$	6.8/5.6/4.8	7.4/6.1/5.2	8.1/6.7/5.8
$T_{\text{e}}(0)/\langle T_{\text{e}} \rangle$ (keV)	20.7/12.0	20.1/11.4	19.4/10.7
$T_{\text{i}}(0)/\langle T_{\text{i}} \rangle$ (keV)	22.5/11.8	21.2/11.2	19.7/10.3
$P_{\text{fus}} \text{ (MW)}/Q$	323.3/6.10	346.4/6.54	385.9/7.28
Divertor material	Be	Be	Be
$Z_{\text{eff}}$	1.32	1.31	1.20
$P_{\text{IT}}/P_{\text{OT}}$ (MW m <sup>-2</sup> )	11.5/16.7	8.7/14.8	9.8/9.5
$P_{\text{sep}}/P_{\text{rad,core}}/P_{\text{rad,div}}$ (MW)	99.5/0.4/18.9	103.1/0.6/18.8	104.4/0.5/16.5

**Table 11.** Summary of results from section 6.1 (W divertor). Main plasma parameters achievable for different fuelling and heating assumptions in an ITER D-T H-mode plasma at 15 MA/5.3 T and 53 MW of additional power.

Case	A	B	C	D
$P_{\text{NBI}}/P_{\text{ECRH}}/P_{\text{ICRH}}$ (MW)	33/-/20	33/-/20	33/-/20	33/-/20
$\Gamma_{\text{D-T}} (10^{22} \text{ s}^{-1})/\Gamma_{\text{Ne}} (10^{20} \text{ s}^{-1})$	1.0/-	2.0/-	3.0/-	4.0/-
$f_{\text{G}}$	0.54	0.70	0.85	0.87
$H_{98}$	0.94	0.89	0.87	0.87
$n_{\text{e}}(0)/\langle n_{\text{e}} \rangle/n_{\text{e,sep}} (10^{19} \text{ m}^{-3})$	7.9/6.4/5.2	10.0/8.1/6.8	12.0/9.9/8.3	12.4/10.2/8.6
$T_{\text{e}}(0)/\langle T_{\text{e}} \rangle$ (keV)	21.0/11.7	18.8/9.8	17.2/8.6	17.1/8.5
$T_{\text{i}}(0)/\langle T_{\text{i}} \rangle$ (keV)	21.0/11.1	17.9/9.3	16.1/8.2	15.9/8.1
$P_{\text{fus}} \text{ (MW)}/Q$	443.3/8.36	520.0/9.81	591.5/11.16	608.2/11.48
Divertor material	W	W	W	W
$Z_{\text{eff}}$	1.01	1.02	1.01	1.01
$P_{\text{IT}}/P_{\text{OT}}$ (MW m <sup>-2</sup> )	14.0/25.0	8.8/19.0	12.3/8.3	8.6/8.1
$P_{\text{sep}}/P_{\text{rad,core}}/P_{\text{rad,div}}$ (MW)	126.5/0.1/0.2	137.0/0.3/0.8	145.1/0.3/0.6	146.8/0.3/0.8

gas fuelling to  $1.0 \cdot 10^{22} \text{ s}^{-1}$  the electron temperature at the targets clearly drops. This shows that in order to achieve radiative divertor conditions in ITER both a sufficient plasma density and impurity levels are required, in agreement with previous studies [30]. Although these simulations did not meet the aim of reducing the target power loads to the projected  $5 \text{ MW m}^{-2}$ , the power load on the divertor target is acceptable from the ITER divertor power load point of view.

#### 5.4. Results at 10 MA/5.3 T/53 MW. Sensitivity to ETB width. (Core modelling only)

The JINTRAC simulations of D-T H-mode plasmas at 10 MA and 5.3 T show significant differences in terms of the predicted fusion performance. This is thought to be due to the strong non-linear dependence of the fusion power on the ion temperature at  $T_{\text{i}} \approx 10 \text{ keV}$  in the plasma core, which is the typical value for the scenario at 10 MA and 5.3 T. To show that this is indeed the case 1.5 dimensional core transport simulations were carried out with JETTO with varying ETB conditions and assumptions for the current density, particle pinch and the auxiliary heating scheme.

The boundary conditions at the separatrix for this series of simulations were taken from a full JINTRAC simulation of a

purely gas fuelled D-T H-mode plasma at 10 MA and 5.3 T with  $P_{\text{aux}} = 53 \text{ MW}$  (including 20 MW of ICRH) applying a constant D-T puff rate of  $1.5 \cdot 10^{22} \text{ s}^{-1}$  and no Ne seeding. In terms of the normalized toroidal flux  $\rho$ , the width of the ETB was varied in the range 0.06–0.08 at constant  $\alpha_{\text{c}}$ , corresponding to a scan in pedestal pressure  $p_{\text{ped}}$  in the range 50–70 kPa. The auxiliary heating was kept at a fixed total power of 53 MW, but either 20 MW of ECRH or ICRH power were applied. Simulations were initialized with different current density profiles corresponding to internal inductance  $l_{\text{i}}(3) = 0.50$  and  $l_{\text{i}}(3) = 0.68$ , respectively. A final simulation was carried out in which a collisionality dependence on the main ion pinch term was taken into account. The results are summarized in tables 8 and 9.

According to the results of the JETTO simulations, the fusion power obtained at 10 MA and 5.3 T can vary between 20–120 MW, corresponding to  $Q$  in the range 0.3–2.3. Due to direct heating of core ions with ICRH giving higher core ion temperatures, the fusion power increases by  $\sim 40 \text{ MW}$  when ECRH is replaced by ICRH with  $^3\text{He}$  minority heating. This is due to the direct heating of ions with this ICRH scheme that increases the ion temperature, marginal at this current for significant fusion power, above 10 keV, thus increasing markedly the fusion power produced.

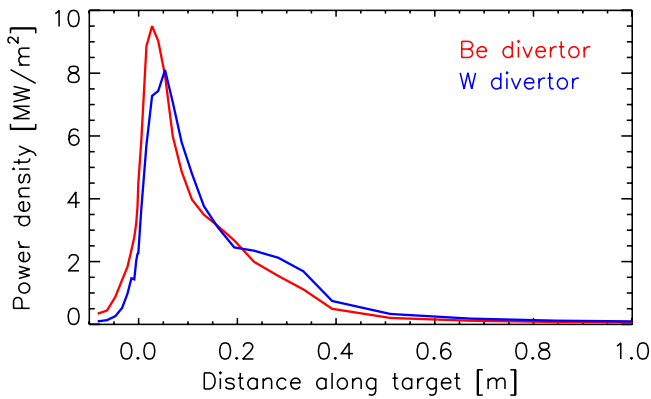


**Figure 12.** Outer target power density profile for case C in table 10 (red, Be divertor) and case D in table 11 (blue, W divertor). The simulations are described in section 6.1  $I_p = 15$  MA,  $B_T = 5.3$  T,  $P_{aux} = 53$  MW, Be and W divertor comparison.

The effect of the collisionality dependence of the particle pinch appears to be negligible, as the collisionality is already very low in 10 MA H-mode plasmas. For an increase of the width of 0.02 in terms of  $\rho$  or, in other terms, for an increase in pedestal pressure of  $\sim 20$  kPa, the fusion power is almost doubled. It should be noted that, because of the dependence of the anomalous transport on the safety factor, the fusion performance is also significantly affected by the shape of the current density profile.

## 6. Results at 15 MA

The bulk of the simulations performed for this study were done at 15 MA, 5.3 T and 53 MW of heating power. In this section we present a series of scans and sensitivity studies performed to analyse the fuelling of this scenario.

### 6.1. Results at 15 MA/5.3 T/53 MW. Be and W divertor

The first series of simulation was a series of JINTRAC runs performed for different gas rates both with Be and W divertor. The results are summarized in tables 10 and 11, whereas in figure 12 we plot typical outer divertor power density profiles for the highest fuelling rates achievable with Be and W divertor respectively.

It can be seen that for these simulations relatively high gas puff rates ( $3.0 \cdot 10^{22} \text{ s}^{-1}$  for Be divertor and  $4.0 \cdot 10^{22} \text{ s}^{-1}$  for a W divertor) can be applied without lowering the temperature at the divertor targets to the point of detachment. This is due to the fact that the increased fusion power amplifies the heat flux crossing the separatrix, which maintains the divertor plasma away from detachment. The presence of an anomalous inward pinch in the core, due to the low plasma collisionality, also plays a role and leads to peaked core density profiles allowing to reach by gas fuelling only a volume-average electron density of  $6\text{--}7 \cdot 10^{19} \text{ m}^{-3}$  in the Be divertor case and  $6\text{--}10 \cdot 10^{19} \text{ m}^{-3}$  in the W divertor case. In the simulations presented here the density at the separatrix was predicted to be in the range  $4.8\text{--}8.6 \cdot 10^{19} \text{ m}^{-3}$ .

In the same simulations, the pressure at the top of the pedestal is  $\sim 120\text{--}125$  kPa, which is in good agreement with

estimates from edge MHD stability modelling for ITER [20, 31]. Interestingly, for these gas fuelled plasmas, the pressure increase in the pedestal zone is due almost exclusively to the large temperature gradient in the ETB, as the density profile in the ETB is almost flat. This is a consequence of the negligible neutral penetration across the separatrix into the core plasma and the lack of an anomalous pinch velocity in the ETB region assumed in this modelling. The results show that for a gas fuelling level of  $3.0 \cdot 10^{22} \text{ s}^{-1}$ ,  $Q \approx 7.5$  in the case of a Be divertor and  $Q \approx 11.0$  in the case of a W divertor could be achieved, even if the effective core fuelling by neutrals remains at a level of  $1.0 \cdot 10^{21} \text{ s}^{-1}$ .

This high fusion performance without core fuelling by pellets with a W divertor is obtained partly because in the simulations we do not consider W sputtering and the He produced by fusion reactions, therefore achieving practically pure plasmas. Moreover, it is assumed in the simulations that the maximum separatrix density achievable by gas fuelling is only determined by the detachment limit in ITER H-modes and that increasing gas fuelling has no influence on the maximum pressure that can be achieved in the H-mode pedestal. Present experiments in H-mode plasmas show that increasing the plasma density by gas fuelling tends to decrease the pedestal pressure and the overall energy confinement in H-mode, which can be due to the increased plasma collisionality affecting the edge current magnitude and therefore the edge MHD stability or to the increased neutral penetration increasing transport in the ETB. Moreover, it has been pointed out that peeling-ballooning stability may impose a limit to the Greenwald fraction achievable at the separatrix, whereby  $f_{G,sep} \leq 0.4\text{--}0.5$  [32]. Therefore, simulations predicting a density at the separatrix exceeding this value may be regarded as unrealistic. However, it is presently unknown if such behaviour will be found in ITER or not, as some of the physics mechanisms invoked to explain present experimental results (i.e. decreased edge current density due to high collisionality or large core plasma neutral source) are not expected to play a significant role in ITER.

It is also important to note that these optimistic results for the core density and  $Q$  achievable in ITER 15 MA plasmas with gas puffing rely on the presence of an anomalous pinch in the core, and, even more importantly, on assumptions of the reduction of anomalous transport in the SOL in H-mode plasmas. In these simulations it is assumed that the reduction of anomalous transport observed in the ETB slightly extends into the SOL. This is observed in present-day experiments and it is the physics mechanism invoked to explain the scaling of the SOL power deposition width in H-modes observed experimentally [33]. Without extension of at least a few millimetres of the low transport domain of the ETB beyond the separatrix, the heat flux would spread over a wider area on the target plates, due to the increased perpendicular transport, and detachment would be reached at much lower gas flux rates. This particular choice for the reduction of transport in the SOL of H-mode plasmas and the level of impurities at the divertor, which contribute to radiated power losses and to the decrease of the divertor temperature affecting the onset of the detachment, allows us to achieve a much higher level for

**Table 12.** Summary of results from section 6.2 (Ne seeding). Main plasma parameters achievable for different fuelling schemes in an ITER D-T H-mode plasma at 15 MA/5.3 T and 53 MW of additional power.

Case	A	B	C	D	E
$P_{\text{NBI}}/P_{\text{ECRH}}/P_{\text{ICRH}}$ (MW)	33/-/20	33/-/20	33/-/20	33/-/20	33/0/20
$\Gamma_{\text{D-T}} (10^{22} \text{ s}^{-1})/\Gamma_{\text{Ne}} (10^{20} \text{ s}^{-1})$	1.0/0.010	1.0/0.075	1.0/0.100	1.0/0.125	3.0/0.010
$f_{\text{G}}$	0.56	0.57	0.47	0.38	0.90
$H_{98}$	0.92	0.93	0.97	1.02	0.86
$n_{\text{e}}(0)/\langle n_{\text{e}} \rangle/n_{\text{e,sep}} (10^{19} \text{ m}^{-3})$	8.3/6.7/5.5	8.4/6.8/5.6	7.4/5.8/4.6	6.1/4.8/3.6	13.0/ 10.6/8.9
$T_{\text{e}}(0)/\langle T_{\text{e}} \rangle$ (keV)	20.5/11.2	20.1/11.1	21.4/12.6	23.0/14.4	17.0/8.4
$T_{\text{i}}(0)/\langle T_{\text{i}} \rangle$ (keV)	20.3/10.6	20.1/10.6	22.9/12.4	27.3/15.0	15.8/8.0
$P_{\text{fus}} (\text{MW})/Q$	456.5/8.61	448.2/8.46	385.0/7.27	312.5/5.90	624.5/11.78
Divertor material	W	W	W	W	W
$Z_{\text{eff}}$	1.0	1.2	1.5	1.9	1.02
$P_{\text{IT}}/P_{\text{OT}} (\text{MW m}^{-2})$	15.0/27.0	16.5/13.0	9.0/9.0	4.0/14.9	14.0/8.4
$P_{\text{sep}}/P_{\text{rad,core}}/P_{\text{rad,div}} (\text{MW})$	129.5/0.4/1.9	127.7/2.3/16.5	121.6/4.8/30.7	111.6/6.1/26.3	156.8/0.5/6.7

the separatrix densities compared to original ITER studies [6]. These were performed with larger anomalous transport coefficients (uniform in the SOL) and C impurities. More recent studies carried out with transport coefficients similar to those in the integrated modelling presented here show similar values for the saturation of the separatrix density in ITER to those reported here [8].

The achievable separatrix density before the onset of detachment is also influenced by the presence of W (the dynamics of which is not considered in the study presented in this paper) and the puffing of Ne because of the associated increase of plasma radiative losses in the core and the SOL. It should be noted that large radiative losses are expected to be required in ITER for high Q D-T plasmas to maintain the peak divertor heat load below  $10 \text{ MW m}^{-2}$ . According to estimates of the power density impinging on the inner and outer target, reducing the peak divertor heat load under this limit requires gas fuelling levels higher than  $2.0 \cdot 10^{22} \text{ s}^{-1}$  in addition to some level of Ne seeding compatible with a core Ne concentrations  $\leq 0.5\%$ .

It should be stressed that, before final conclusions for ITER can be drawn, a detailed quantitative validation of the integrated modelling approach applied to ITER with experimental results from gas fuelled H-mode density scans in present experiments is required. In the case of H-mode conditions this requires not only the validation of the SOL modelling assumptions setting the maximum achievable separatrix density, but also of the MHD stability and transport assumptions in the ETB for H-mode plasmas with high plasma density, low pedestal collisionality and low neutral source in the pedestal region which require dedicated experiments at the highest currents and powers achievable in existing tokamaks to approach these ITER-like conditions.

### 6.2. Results at 15 MA/5.3 T/53 MW. Impurity seeding to reduce divertor power load below $10 \text{ MW m}^{-2}$

In the second scan performed for a 15 MA ITER H-mode D-T plasma, the JINTRAC simulations for purely gas fuelled H-mode plasmas at 15 MA, 5.3 T, 53 MW of auxiliary heating and a W divertor presented in section 6.1 were continued at

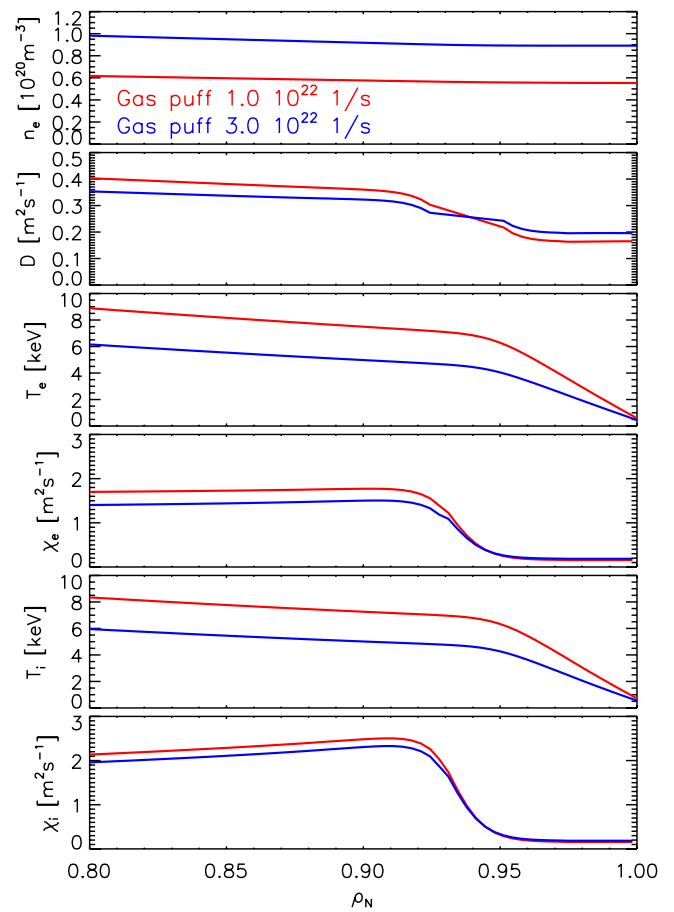


**Figure 13.** Ne seeding simulations (section 6.2). Core plasma electron density, particle diffusivity, electron temperature, electron heat conductivity, ion temperature and ion heat conductivity profiles for case A (red) and E (blue) in table 12.  $I_p = 15 \text{ MA}$ ,  $B_T = 5.3 \text{ T}$ ,  $P_{\text{aux}} = 53 \text{ MW}$ .

fixed D-T gas puff rates of either  $1.0 \cdot 10^{22} \text{ s}^{-1}$  or  $3.0 \cdot 10^{22} \text{ s}^{-1}$  switching on Ne seeding at various levels in order to perform a scan in Ne gas puff rates. Ne seeding was applied from both divertor target plates, while D-T gas was inserted in the main chamber from the top of the vessel. The results are summarized in table 12. In figures 13 and 14 we show the electron density, particle diffusivity, electron temperature, electron

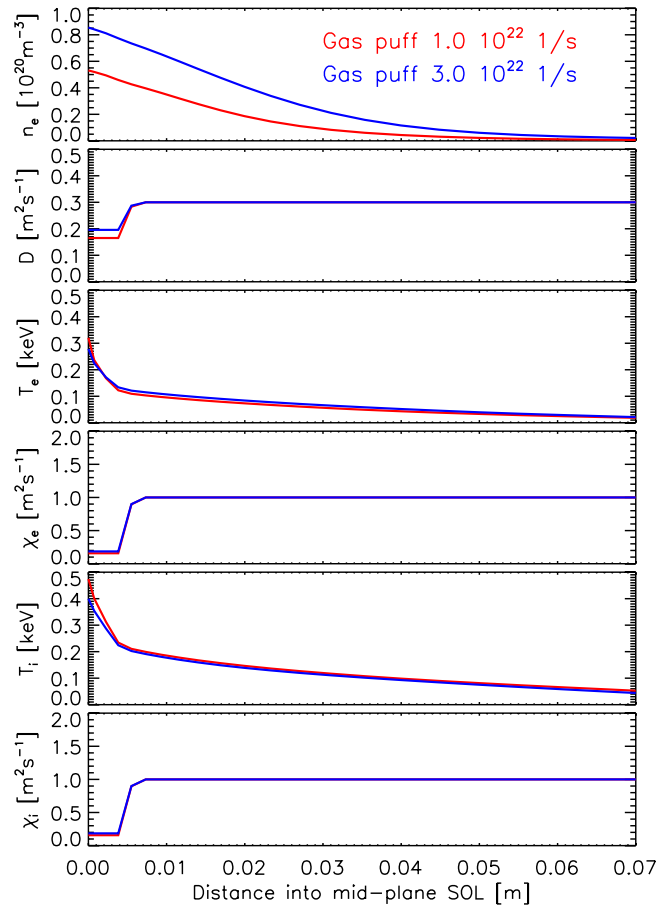


**Figure 14.** Ne seeding simulations (section 6.2). Mid-plane SOL electron density, particle diffusivity, electron temperature, electron heat conductivity, ion temperature and ion heat conductivity profiles for case A (red) and B (blue) in table 12.  $I_p = 15$  MA,  $B_T = 5.3$  T,  $P_{aux} = 53$  MW.

heat conductivity, ion temperature and ion heat conductivity profiles in the plasma core and in the SOL, respectively. The two cases shown in the figures are for  $\Gamma_{D-T} = 1.0 \cdot 10^{22} \text{ s}^{-1}$  and  $\Gamma_{D-T} = 3.0 \cdot 10^{22} \text{ s}^{-1}$  at fixed  $\Gamma_{Ne} = 1.0 \cdot 10^{18} \text{ s}^{-1}$ .

According to the simulation results, Ne puff rates up to  $\sim 1.5 \cdot 10^{19} \text{ s}^{-1}$  can be continuously applied in quasi-stationary purely gas fuelled H-mode plasmas at D-T gas puff rate of  $\sim 1.0 \cdot 10^{22} \text{ s}^{-1}$ . At higher Ne puff rates, the contamination of the core and SOL by Ne becomes too high and the plasma becomes thermally unstable. At  $\Gamma_{Ne} = 1.25 \cdot 10^{19} \text{ s}^{-1}$ , the Ne concentration in the core already amounts to  $\sim 1\%$  with  $Z_{eff} \sim 1.9$  while the level of Ne radiation in the SOL reaches  $\sim 30\text{--}35$  MW. As expected, the plasma density is reduced with increased impurity contamination of the plasma. For the extreme case with  $\Gamma_{Ne} = 1.25 \cdot 10^{19} \text{ s}^{-1}$ , the volume-average electron density drops from  $6.7 \cdot 10^{19} \text{ m}^{-3}$  to  $4.8 \cdot 10^{19} \text{ m}^{-3}$  and the fusion power is reduced from  $\sim 450$  MW to  $\sim 310$  MW due to plasma dilution.

It should be noted that, at lower D-T gas fuelling rates and lower SOL density, Ne radiates less efficiently and therefore higher Ne gas puff rates are needed and higher Ne core concentrations are reached when the Ne seeding is adjusted to achieve a given level of Ne radiation in the SOL. Moreover, at lower SOL densities, the screening of Ne is reduced, which

further contributes to higher Ne concentrations in the core. In any case, simulation results tend to show that with a Ne puff rate of  $\sim 1.0 \cdot 10^{19} \text{ s}^{-1}$  providing  $\sim 30$  MW of Ne radiation in the SOL, the maximum power density on the inner and outer targets could be reduced below the critical limit of  $10 \text{ MW m}^{-2}$  and  $Z_{eff} \approx 1.5$  could be maintained in the core. However, as a consequence of the low applied D-T gas puff rate, the ion temperature seems to remain above the guideline value of  $\sim 5$  eV for W sputtering by light impurities in vicinity to the strike points where a peak in ion current density is expected.

It is interesting to note that the peak power density on the outer target does not monotonically decrease for increased Ne puff rates. For  $\Gamma_{Ne} = 1.25 \cdot 10^{19} \text{ s}^{-1}$ , the peak power density is larger than the one obtained with  $\Gamma_{Ne} = 1.0 \cdot 10^{19} \text{ s}^{-1}$ . This trend reversal seems to be related to transport assumptions for the ETB and the SOL. As the density is reduced at increased  $\Gamma_{Ne}$ , the pressure on top of the pedestal is maintained roughly constant by the continuous ELM model with fixed  $\alpha_c$ . Therefore, the temperature gradient increases, while the heat flux from the core tends to decrease because of the increased dilution and core radiated power. For this reason, the electron heat diffusivity must become lower for higher  $\Gamma_{Ne}$ . This eventually leads to a reduced spread in heat deposition on the target causing larger power density peak values in vicinity to the strike points, although the total deposited power may actually be lower with increased Ne puff.

Comparing two cases with the same Ne puff rate  $\Gamma_{Ne} = 1.0 \cdot 10^{18} \text{ s}^{-1}$  with low and high D-T gas puff rates of  $\Gamma_{D-T} = 1.0 \cdot 10^{22} \text{ s}^{-1}$  and  $\Gamma_{D-T} = 3.0 \cdot 10^{22} \text{ s}^{-1}$ , the effect of enhanced Ne dissipation to the core for reduced  $\Gamma_{D-T}$  can be illustrated. As shown in table 12, the plasma core and edge densities are enhanced and the plasma approaches detached conditions at  $\Gamma_{D-T} = 3.0 \cdot 10^{22} \text{ s}^{-1}$ , but the Ne content in the core remains lower ( $\sim 1.4 \cdot 10^{19}$  Ne atoms) compared to the case with  $\Gamma_{D-T} = 1.0 \cdot 10^{22} \text{ s}^{-1}$  ( $\sim 2.0 \cdot 10^{19}$  Ne atoms). The Ne can be kept near the targets more efficiently with increased D-T gas fuelling due to an enhanced transfer of target-directed momentum from main ions to Ne particles via collisions in a high density environment.

### 6.3. Results at 15 MA/5.3 T/53 MW. Continuous pellet fuelling

As illustrated by the previous two series of simulations and the issues related to the achievement of high confinement with flat density profiles in the pedestal, gas fuelling is likely to be insufficient to achieve high fusion performance  $Q \approx 10$  and the required core densities. However, pellet fuelling can provide a way to achieve high plasma core average densities near the Greenwald density limit while the separatrix density can be kept at values which are expected to be compatible with high pedestal pressure and high energy confinement.

To investigate plasma operation in ELMy H-mode at high core density close to  $Q \approx 10$ , simulations were carried out for the flat-top phase of the ITER baseline scenario at 15 MA, 5.3 T and with W target using the continuous pellet fuelling model, continuing from a case in which the density in the

**Table 13.** Summary of results from section 6.3 (continuous pellet model). Main plasma parameters achievable for different fuelling, heating and transport model assumptions in an ITER D-T H-mode plasma at 15 MA/5.3 T and 53 MW of additional power.  $\rho_p$  is the radial location of the barycentre (in terms of normalized toroidal flux),  $\Delta_p$  is the full width at half maximum and  $\Gamma_p$  is the time averaged intensity of the pellet particle source introduced in these simulations, which has a Gaussian radial profile.

Case	A	B	C
$P_{\text{NBI}}/P_{\text{ECRH}}/P_{\text{ICRH}}$ (MW)	33/20/–	33/20/–	33/20/–
$\Gamma_{\text{D-T}} (10^{22} \text{ s}^{-1})/\Gamma_{\text{Ne}} (10^{20} \text{ s}^{-1})$	–/–	–/–	1.0/1.0
$\rho_p/\Delta_p/\Gamma_p (10^{21} \text{ s}^{-1})$	0.85/0.2/12.0	0.85/0.2/12.1	0.85/0.2/9.2
$f_G$	0.90	0.89	0.90
$H_{98}$	0.87	0.92	0.89
$n_e(0)/\langle n_e \rangle/n_{e,\text{sep}} (10^{19} \text{ m}^{-3})$	13.2/10.4/ 5.6	13.3/10.5/ 5.8	13.4/10.7/ 5.9
$T_e(0)/\langle T_e \rangle$ (keV)	16.0/ 8.2	20.9/ 8.2	16.0/ 8.5
$T_i(0)/\langle T_i \rangle$ (keV)	14.0/ 7.7	17.7/ 7.7	14.0/ 7.8
$P_{\text{fus}} (\text{MW})/Q$	460.7/8.69	478.9/9.04	499.8/ 9.43
Divertor material	W	W	W
$Z_{\text{eff}}$	1.3	1.3	1.2
$P_{\text{IT}}/P_{\text{OT}} (\text{MW m}^{-2})$	25.0/38.0	16.8/30.0	5.5/12.0
$P_{\text{sep}}/P_{\text{rad,core}}/P_{\text{rad,div}} (\text{MW})$	104.1/2.3/4.6	104.4/2.3/4.1	118.0/19.8/28.7
Core transport model	Bohm/gyro-Bohm	GLF23	Bohm/gyro-Bohm

core is already close to stationary conditions. 33 MW of NB heating and 20 MW of ECRH are applied to the plasma. D-T gas puff has either been completely switched off or set to fixed level of  $1.0 \cdot 10^{22} \text{ s}^{-1}$ . Pellets are assumed to be injected from the high-field side (HFS) of the torus with a deposition profile centred at  $\rho = 0.85$ . A continuous pellet particle source profile with Gaussian shape and profile width of 0.2 in terms of  $\rho$  is applied and rescaled to a given total particle source rate that is feedback controlled to maintain the line-averaged electron density close to a target value of  $1.05 \cdot 10^{20} \text{ m}^{-3}$ , which corresponds to 85%–90% of the Greenwald density limit. The width and the depth of the pellet source profile have been chosen to mimic typical pellet deposition profiles calculated for this target plasma by the HPI2 ablation/deposition code.

The initial applied total pellet particle source rate amounts to  $7.5 \cdot 10^{21} \text{ s}^{-1}$ . The core transport for  $\rho < 0.9$  has either been modelled with the Bohm/gyro-Bohm model plus the ‘ad hoc’ inward particle pinch described earlier in the paper or with GLF23. For  $\rho > 0.9$  the Bohm/gyro-Bohm model has been applied in all cases. The model assumptions applied for the transport prediction in the ETB and SOL are the same as in the previous series of simulations. Be and Ne transport was taken into account. The applied Ne puff rate was varied during the simulations in order to achieve a scan between configurations with low Ne SOL radiation in the order of  $\sim 5$  MW and high Ne SOL radiation of up to  $\sim 30$ – $35$  MW.

The main simulation results are summarized in table 13. The simulations indicate that a burning regime at high density approaching the ITER target of  $Q \approx 10$  could be achieved with pellet fuelling. With the selected heating and fuelling configuration, the fusion power is predicted to vary around  $\sim 480$  MW, corresponding to  $Q \approx 9.0$ . The comparison of predictions with different core transport models demonstrates that GLF23 predictions are in reasonable agreement with the modified Bohm/gyro-Bohm model for high performance plasmas at  $Q \leq 10$  in this ITER baseline scenario. In particular the prediction of the density peaking matches

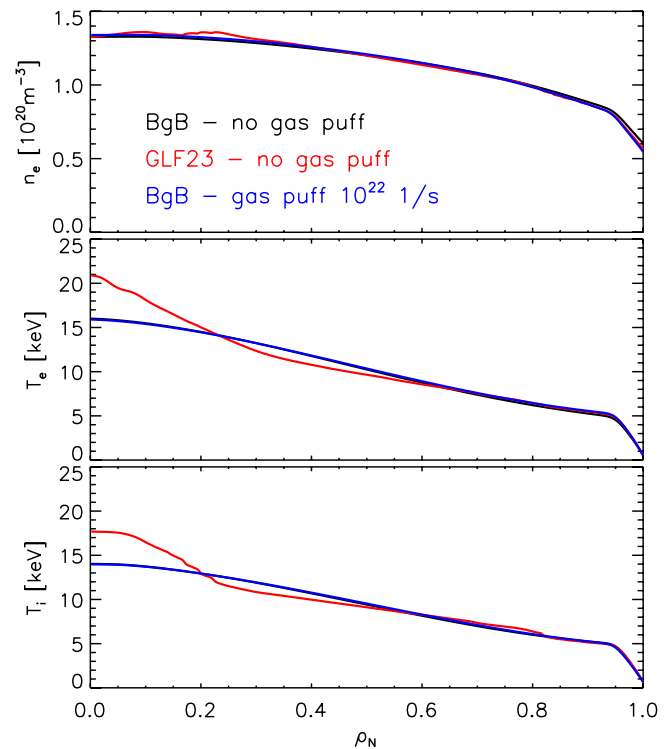


**Figure 15.** Comparison of electron density and temperature profiles for a quasi-stationary pellet fuelled burning H-mode plasma at 15 MA/5.3 T, with 33 MW of NB and 20 MW of ICRH and  $Q \approx 10$  with core transport modelled with either the GLF23-like Bohm/gyro-Bohm model (black) or the GLF23 model (red). In these cases there is no D-T gas puff and Ne radiation in the SOL amounts only to a few MW. A third case with  $\Gamma_{\text{D-T}} = 10^{22} \text{ s}^{-1}$  is also shown for comparison (blue).

well, while some differences can be observed in the details of the temperature profiles, with GLF23 predicting a steeper temperature gradient in the core and a shallower gradient further outside. The difference between the temperature profiles inside  $\rho \approx 0.2$  can be attributed to the fact that GLF23 tends to predict almost no turbulence and, consequently, very low

**Table 14.** Summary of results from section 6.4 (discrete pellet mass scan, Ne seeding). Main plasma parameters achievable for different pellet sizes and frequencies in an ITER D-T H-mode plasma at 15 MA/5.3 T and 53 MW of additional power.  $m_p$  and  $f_p$  are the pellet mass and frequency respectively.

Case	A	B	C	D	E
$P_{\text{NBI}}/P_{\text{ECRH}}/P_{\text{ICRH}}$ (MW)	33/20/–	33/20/–	33/20/–	33/20/–	33/20/–
$\Gamma_{\text{D-T}} (10^{22} \text{ s}^{-1})/\Gamma_{\text{Ne}} (10^{20} \text{ s}^{-1})$	1.0/0.01	1.0/0.01	1.0/0.01	1.0/0.01	1.0/0.01
$m_p (10^{21} \text{ atoms})/f_p$ (Hz)	2.0/3.6	2.7/2.5	3.5/2.3	4.4/2.1	5.5/1.4
$f_G$	0.85	0.85	0.88	0.85	0.88
$H_{98}$	0.91	0.91	0.92	0.91	0.92
$n_e(0)/\langle n_e \rangle/n_{e,\text{sep}} (10^{19} \text{ m}^{-3})$	13.1/10.1/5.5	13.1/10.2/5.5	13.2/10.2/5.5	13.2/10.3/5.5	13.2/10.3/5.5
$T_e(0)/\langle T_e \rangle$ (keV)	16.4/8.7	16.3/8.7	16.3/8.5	16.2/8.7	16.2/8.5
$T_i(0)/\langle T_i \rangle$ (keV)	14.4/8.3	14.4/8.2	14.4/8.0	14.3/8.2	14.3/8.0
$P_{\text{fus}} (\text{MW})/Q$	530.6/10.01	529.6/9.99	531.2/10.02	541.3/10.21	538.7/10.17
Divertor material	W	W	W	W	W
$Z_{\text{eff}}$	1.7	1.7	1.6	1.7	1.6
$P_{\text{IT}}/P_{\text{OT}} (\text{MW m}^{-2})$	4.1/8.4	4.7/8.5	4.0/6.4	4.4/7.8	4.5/9.0
$P_{\text{sep}}/P_{\text{rad,core}}/P_{\text{rad,div}} (\text{MW})$	124.5/14.8/58.4	124.4/14.8/57.6	124.1/14.8/57.2	123.9/14.9/60.9	123.4/14.9/56.9

**Table 15.** Summary of results from section 6.4 (discrete pellet frequency scan, Ne seeding). Main plasma parameters achievable for different pellet frequencies in an ITER D-T H-mode plasma at 15 MA/5.3 T and 53 MW of additional power. In this table,  $\langle \dot{n}_e \rangle$  is the secular increase in volume-average density resulting from pellet injection.

Case	A	B	C	D
$P_{\text{NBI}}/P_{\text{ECRH}}/P_{\text{ICRH}}$ (MW)	33/20/–	33/20/–	33/20/–	33/20/–
$\Gamma_{\text{D-T}} (10^{22} \text{ s}^{-1})/\Gamma_{\text{Ne}} (10^{20} \text{ s}^{-1})$	1.0/0.01	1.0/0.01	1.0/0.01	1.0/0.01
$m_p (10^{21} \text{ atoms})/f_p$ (Hz)	4.4/3.5	4.4/4.0	4.4/4.5	4.4/5.0
$\langle \dot{n}_e \rangle (10^{18} \text{ m}^{-3} \text{ s}^{-1})$	1.0	1.6	4.0	5.6
$f_G$	0.85	0.85	0.88	0.94
$n_e(0)/\langle n_e \rangle/n_{e,\text{sep}} (10^{19} \text{ m}^{-3})$	13.5/10.0/4.4	13.5/10.0/4.3	13.8/10.5/4.4	14.3/11.2/4.5
$T_e(0)/\langle T_e \rangle$ (keV)	16.8/10.1	16.9/9.2	16.9/9.5	16.7/9.0
$T_i(0)/\langle T_i \rangle$ (keV)	15.8/9.7	14.9/8.7	15.0/8.8	15.0/8.5
$P_{\text{fus}} (\text{MW})/Q$	670.0/12.64	585.0/11.03	635.0/11.98	685.0/12.92
Divertor material	W	W	W	W
$Z_{\text{eff}}$	1.7	1.6	1.6	1.6
$P_{\text{IT}}/P_{\text{OT}} (\text{MW m}^{-2})$	6.2/10.4	4.2/7.5	4.3/6.0	4.1/6.4
$P_{\text{sep}}/P_{\text{rad,core}}/P_{\text{rad,div}} (\text{MW})$	120.2/33.1/63.4	121.7/31.0/59.4	119.1/32.5/62.3	117.5/34.1/65.3

transport in this region of the plasma. The core electron density and electron and ion temperature profiles are shown in figure 15. It should also be noted that, in the case of GLF23 transport model, the predicted peak power density on the inner and outer divertor is respectively 33% and 21% lower than in the case of the Bohm/gyro-Bohm transport model.

Without any D-T gas fuelling and low Ne radiation in the SOL of only a few MW, the peak power density on the outer target is estimated to be in a range of 25–40 MW m<sup>-2</sup> (table 13 cases A and B). In addition,  $T_i > 5$  eV everywhere on the targets except for the area interacting with the private region. Gas fuelling and Ne seeding seem to be mandatory to protect the target plates in the burning high  $Q$  regime. According to simulation results (table 13 case C), the power density can be reduced to 12 MW m<sup>-2</sup> on the outer divertor and 5.5 MW m<sup>-2</sup> on the inner divertor and the ion temperature is reduced below 5 eV in regions with maximum ion current density for a constant D-T gas puff rate of  $1.0 \cdot 10^{22} \text{ s}^{-1}$  and Ne puff

adjustment to reach a Ne SOL radiation level of 30–35 MW ( $\Gamma_{\text{Ne}} \approx 1.0 \cdot 10^{20} \text{ s}^{-1}$ ). To maintain the core density at a constant level of 85%–90% of the Greenwald density limit in the quasi-stationary flat-top phase of the ITER 15 MA baseline scenario, a D-T pellet particle fuelling rate of  $\sim 1.0 \cdot 10^{22} \text{ s}^{-1}$  is required.

#### 6.4. Results at 15 MA/5.3 T/53 MW. Discrete pellet and impurity seeding

Although modelling pellet injection with the continuous pellet model can give some insight of what are the differences expected when the depth of the particle source is changed, it does not capture the intermittent nature of the pellet and the finite material retention time following the injection of a pellet. To model pellet fuelling in a more realistic way a discrete pellet model was used also for this scenario similarly to what was done for the 7.5 MA and 10 MA scenarios.

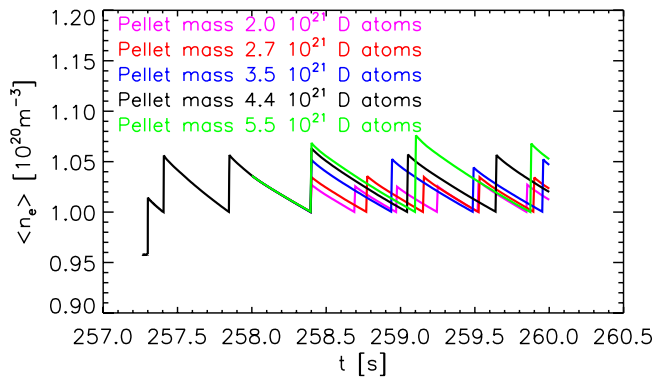


**Figure 16.** Evolution and control of the plasma volume-average density by means of pellet injection in 15 MA/5.3 T ITER D-T baseline H-mode with 33 MW of NB and 20 MW of ICRH for a target volume-average density of  $10^{20} \text{ m}^{-3}$  and with different levels of back-ground gas puff. The target densities are easily achieved and maintained.

The main purpose of this group of simulations was to model the fuelling of a 15 MA, 5.3 T ITER D-T baseline H-mode with discrete pellets of various sizes to obtain  $Q = 10$  and simultaneously find the maximum pellet size with acceptable divertor power load between pellets.

The cases analyzed and summarized in tables 14 and 15 were the continuation of a simulation with continuous pellets, background D-T gas puff  $1.0 \cdot 10^{22} \text{ s}^{-1}$  from the main chamber and  $1.0 \cdot 10^{20} \text{ s}^{-1}$  Ne seeding from the divertor region, which reached a volume-average density of  $9.6 \cdot 10^{19} \text{ m}^{-3}$ . The reference simulation was continued for 2.5 s by replacing continuous with discrete pellets of mass  $4.4 \cdot 10^{21}$  atoms, speed  $300 \text{ m s}^{-1}$ , composition 50–50 D-T and requiring the plasma volume-averaged density to be maintained at  $1.0 \cdot 10^{20} \text{ m}^{-3}$ . It can be seen from figure 16 that two pellets fired at a frequency of  $\sim 6.5 \text{ Hz}$  are needed to bring the volume-average density from the initial to the target value. Once the target value has been reached a pellet injection frequency of  $\sim 2.1 \text{ Hz}$  is needed to maintain the required volume-average density.

In order to explore the sensitivity of the simulation to the pellet mass and injection frequency, we performed two scans. In the first scan, starting from one second into the phase of the simulation where discrete pellets were used, we varied the pellet radius and injected pellets of mass  $2.0 \cdot 10^{21}$ ,  $2.7 \cdot 10^{21}$ ,  $3.5 \cdot 10^{21}$ ,  $4.4 \cdot 10^{21}$  and  $5.5 \cdot 10^{21}$  atoms. For pellet masses above  $5.5 \cdot 10^{21}$  atoms, the fuelling load imposed on the plasma was too high, the divertor reached a detached state shortly after the start of the run and the simulation could not be carried on until the end. However, delaying the injection of the first pellet by 0.5 s and allowing the density to decrease, made possible the injection of pellets of mass  $6.1 \cdot 10^{21}$  atoms. This indicates that there is a maximum pellet mass allowed to avoid divertor detachment and that its value is sensitive to the pre-pellet density.

The evolution of the electron density and temperature at the divertor plates, together with the evolution of the volume-average electron density in the plasma core are shown in figure 17 for the case with pellet mass  $5.5 \cdot 10^{21}$  atoms. It can be seen that each pellet induces a drop in electron density and

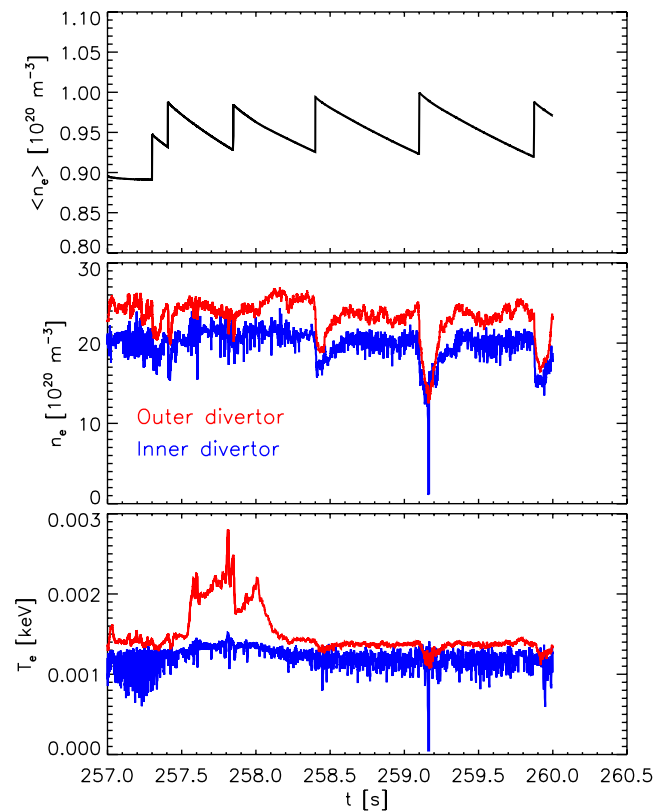


**Figure 17.** Time evolution of the volume-average electron density in the core plasma and the electron density and temperature at the intersection of the separatrix with the outer (red) and inner (blue) divertor target in a 15 MA/5.3 T ITER D-T baseline H-mode with 33 MW of NB and 20 MW of ICRH and pellets of mass  $5.5 \cdot 10^{21}$  atoms injected to achieve a volume-average core plasma electron density of  $10^{20} \text{ m}^{-3}$ .

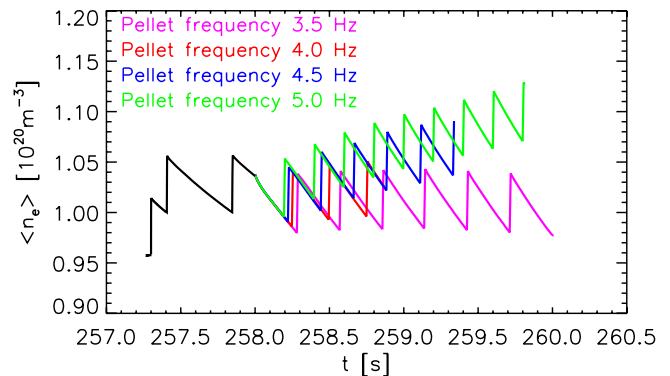


**Figure 18.** Evolution of the plasma volume-average density by means of pellet injection in 15 MA/5.3 T ITER DT baseline H-mode with 33 MW of NB and 20 MW of ICRH for different fixed pellet frequencies.

temperature at the divertor plates pushing these parameter close to the limit where a numerical instability in the simulation is triggered. In all the cases explored, we were able to maintain the required plasma volume-average density, but the pellet frequency needed to do so changes as illustrated in table 14.

In the second scan, we did not require any target volume-average density, but we fixed the pellet mass at  $4.4 \cdot 10^{21}$

**Table 16.** Summary of results from section 6.5 (He accumulation). Main plasma parameters achievable in an ITER D-T H-mode plasma at 15 MA/5.3 T and 53 MW of additional power taking into account He, Be and W as impurities. Case A:  $n_{\text{He}}(\rho = 1) = 5 \cdot 10^{17} \text{ m}^{-3}$ ; case B:  $n_{\text{He}}(\rho = 1) = 6 \cdot 10^{18} \text{ m}^{-3}$ .

Case	A	B
$P_{\text{NBI}}/P_{\text{ECRH}}/P_{\text{ICRH}}$ (MW)	33/20/-	33/20/-
$\Gamma_{\text{D-T}} (10^{22} \text{ s}^{-1})/\Gamma_{\text{Ne}} (10^{20} \text{ s}^{-1})$	1.0/-	1.0/-
$f_{\text{G}}$	0.57	0.66
$H_{98}$	0.96	0.95
$n_{\text{e}}(0)/\langle n_{\text{e}} \rangle/n_{\text{e,sep}} (10^{19} \text{ m}^{-3})$	8.9/6.8/5.3	9.9/7.9/6.4
$n_{\text{He}}/\langle n_{\text{e}} \rangle (\text{core})/n_{\text{He}}/\langle n_{\text{e}} \rangle$ (separatrix)(%)	1.9/0.7	7.5/7.5
$T_{\text{e}}(0)/\langle T_{\text{e}} \rangle$ (keV)	28.4/11.9	26.1/10.6
$T_{\text{i}}(0)/\langle T_{\text{i}} \rangle$ (keV)	20.9/10.7	20.0/10.0
$P_{\text{fus}}$ (MW)/ $Q$	447.9/8.45	401.6/7.58
Divertor material	W	W
$Z_{\text{eff}}$	1.08	1.19

atoms and the pellet speed at  $300 \text{ m s}^{-1}$  and, starting from one second into the phase of the simulation fuelled by discrete pellets, we injected pellet at frequency of 3.5, 4.0, 4.5 and 5.0 Hz. The results for the range of frequencies explored are shown in table 15, where, for each pellet frequency, we report the corresponding rate of increase of the plasma volume-average density. It should be noted that the rate of change of the density cannot be maintained indefinitely, as for a given pellet frequency the plasma volume-average density will saturate at a new equilibrium level. This can be seen in figure 18 for the 3.5 Hz pellets, where, after a barely visible increase caused by the first two pellets, the plasma volume-average density stops increasing and remains just below  $1.0 \cdot 10^{20} \text{ m}^{-3}$ .

As for the divertor power load, in the pellet mass scan it was similar in all the simulations performed and varied from  $4.5 \text{ MW m}^{-2}$  on the inner target to  $9.0 \text{ MW m}^{-2}$  on the outer target. The pellet frequency scan showed more variability and the power load on the divertor plates was  $6.0 \text{ MW m}^{-2}$  on the inner target and  $10 \text{ MW m}^{-2}$  on the outer target for the case with pellet frequency 3.5 Hz and  $4.0 \text{ MW m}^{-2}$  on the inner target and  $6.0 \text{ MW m}^{-2}$  on the outer target for the case with pellet frequency 5.0 Hz (the values for the intermediate cases were between these extremes).

### 6.5. Results at 15 MA/5.3 T/53 MW. He accumulation. (Core modelling only)

In purely gas-fuelled H-mode plasmas with high fusion power production, the removal of the He ashes from the core might be challenging, as the core particle throughput is rather small because of the negligible particle source from the neutral beams and the neutrals penetrating from the edge and because of the particle transport to the SOL might be reduced in the inter-ELM phase due to the small density gradients in the ETB. It is therefore important to investigate whether problems related to He core accumulation such as fuel dilution and energy radiation could become critical in gas fuelled, high  $Q$ , H-mode plasmas.

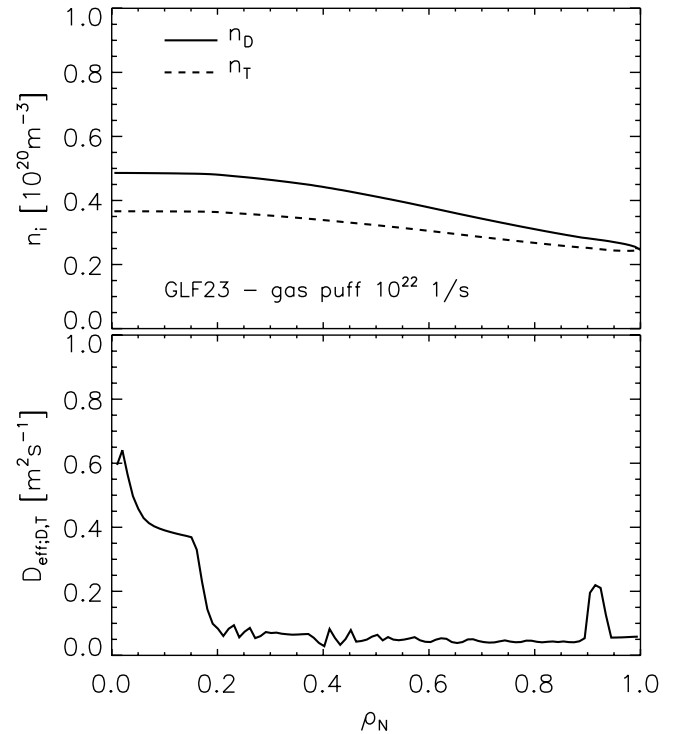


**Figure 19.** He accumulation study (section 6.5). D and T density and effective diffusivity profiles for a JETTO/SANCO core transport simulation with GLF23 and NCLASS taking into account momentum transport of an ITER D-T H-mode plasma at 15 MA/5.3 T with 33 MW of NB and 20 MW of ICRH, W targets, in steady-state conditions. (table 16 case A).

To this end, core transport simulations have been carried out with the JETTO/SANCO code with boundary conditions for the density, the temperature and the D-T neutral influx at the separatrix taken from a full JINTRAC simulation of a purely gas fuelled D-T H-mode plasma with W targets at fixed D-T puff rate  $\Gamma_{\text{D-T}} = 1.0 \cdot 10^{22} \text{ s}^{-1}$  described in section 6.1. The core transport of the three impurities He, Be, and W is considered. The impurity densities are fixed at the separatrix to  $n_{\text{He}} = 5 \cdot 10^{17} \text{ m}^{-3}$ ,  $n_{\text{Be}} = 5 \cdot 10^{17} \text{ m}^{-3}$ ,  $n_{\text{W}} = 5 \cdot 10^{15} \text{ m}^{-3}$ . The impurity neutral influx at the separatrix is assumed to be negligible. This choice for the boundary conditions can be justified by the fact that  $n_{\text{Be}}$  is in line with the lower end of the interval of possible values estimated in [6] for low and high gas puff rates (a run corresponding to the higher end of the scan is discussed later),  $n_{\text{Be}}$  is fitted to obtain the same  $Z_{\text{eff}}$  as in the full JINTRAC simulations on which these JETTO/SANCO runs are based and  $n_{\text{W}}$  is low enough to result in a negligible concentration of W in the core, resulting from a significant temperature screening.

Anomalous core transport is modelled by GLF23, considering impurity specific anomalous particle transport. The continuous sawtooth model is used to model the effect of sawteeth on heat and particle transport in the region affected by sawteeth. According to this model,  $D$  and  $\chi_{i,e}$  are increased (typically to values between  $0.3$  and  $0.4 \text{ m}^2 \text{ s}^{-1}$ ) inside the  $q = 1$  surface to flatten the density and temperature profiles. Moreover, the value of the plasma resistivity at the  $q = 1$  surface is extended inside this region to reduce the current

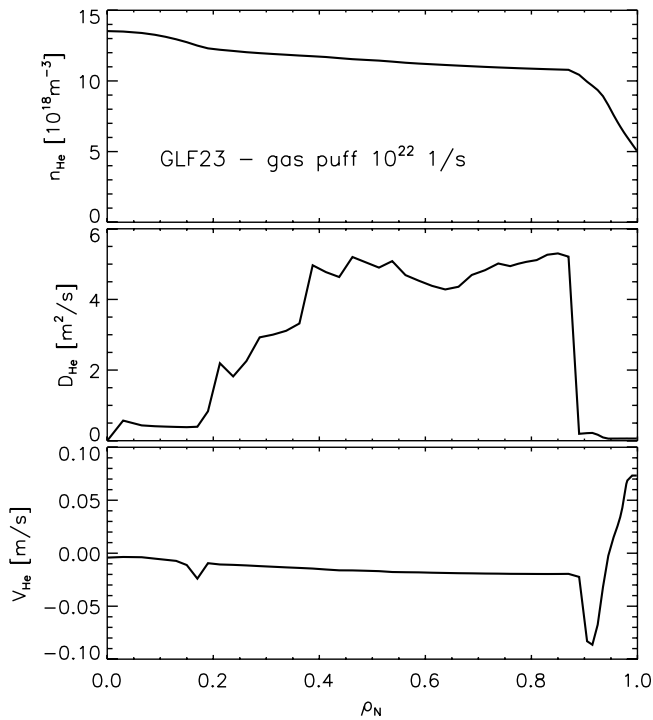


**Figure 20.** He accumulation study (section 6.5). He density, He diffusivity and He convective velocity profiles for a JETTO/SANCO core transport simulation with GLF23 and NCLASS taking into account momentum transport of an ITER D-T H-mode plasma at 15 MA/5.3 T with 33 MW of NB and 20 MW of ICRH, W targets, in steady-state conditions. (table 16 case A).

density in the plasma core and, consequently, increase  $q$  and the flux consumption. The core momentum transport with torque from neutral beams and  $\chi_\phi = \chi_i$  is also taken into account. Because of the stabilising effect of rotational shear on microturbulence, the core confinement is improved and the fusion power increased ( $P_{\text{fus}} \approx 450$  MW) compared to the full JINTRAC simulation (where  $P_{\text{fus}} \approx 400$  MW). This configuration was selected for this study because this is where it is thought that the problems related to He core accumulation can become more apparent, due to the reduction in anomalous core transport and the increased production of He ash from the fusion reaction and operating at low density with a small gas flux rate of  $\Gamma_{\text{D-T}} = 1.0 \cdot 10^{22} \text{ s}^{-1}$ .

The results are summarized in table 16 (case A), from which it can be seen that, in the best performing case,  $Q \approx 9$ . In these conditions, the He ash production rate amounts to  $\sim 1.6 \cdot 10^{20} \text{ s}^{-1}$ . Inspecting the density and effective diffusivity profiles for the main ions (shown in figure 19), it can be seen that GLF23 predicts an anomalous inwards pinch for the main ions. This can be concluded from the fact that the effective diffusivity for D and T is close to zero (and, at times, even negative) across a wide region of the plasma, causing non-zero density gradients for both D and T even in absence of T core sources. On the other side, the anomalous He transport is almost purely diffusive, as it can be seen from figure 20, which shows the He density and the He total diffusivity and convective velocity (neoclassical plus anomalous). Some small fluctuations in He pinch velocity are present in the edge region and can be attributed to neoclassical transport. Although a strong

**Table 17.** Summary of results from section 6.6 (He accumulation with pellet fuelling). Main plasma parameters achievable in an ITER D-T H-mode plasma at 15 MA/5.3 T and 53 MW of additional power taking into account He, Be and W as impurities. Ne seeding adjusted to obtain a fixed level of radiated power in the SOL (case A: 30 MW; case B: 28 MW). The concentration of He in the core is also given.

Case	A	B
$P_{\text{NB1}}/P_{\text{ECRH}}/P_{\text{ICRH}}$ (MW)	33/20/-	33/20/-
$\Gamma_{\text{D-T}}$ ( $10^{22} \text{ s}^{-1}$ )	1.0/0.1	1.0/0.1
$\Gamma_{\text{Ne}}$ ( $10^{20} \text{ s}^{-1}$ )		
$m_p$ ( $10^{21}$ atoms)/ $f_p$ (Hz)	5.5/2.3	5.5/2.4
$f_G$	0.82	0.83
$H_{98}$	0.95	0.93
$n_e(0)/\langle n_e \rangle/n_{e,\text{sep}}$ ( $10^{19} \text{ m}^{-3}$ )	12.5/9.9/5.4	12.6/9.9/5.3
$n_{\text{He}}/\langle n_e \rangle$ (core)/ $n_{\text{He}}/\langle n_e \rangle$ (separatrix) (%)	6.5/2.6	6.3/2.6
$T_e(0)/\langle T_e \rangle$ (keV)	16.7/9.4	16.6/9.2
$T_i(0)/\langle T_i \rangle$ (keV)	14.9/8.8	14.9/8.7
$P_{\text{fus}}$ (MW)/ $Q$	497.3/9.38	482.4/9.10
Divertor material	W	W
$Z_{\text{eff}}$	1.35	1.42
$P_{\text{IT}}/P_{\text{OT}}$ ( $\text{MW m}^{-2}$ )	6.6/5.8	5.5/5.6
$P_{\text{sep}}/P_{\text{rad,core}}/P_{\text{rad,div}}$ (MW)	126.2/25.2/35.6	124.3/26.5/39.9

outward neoclassical pinch is predicted in the ETB region for high  $Z$  impurities, leading to almost complete screening of W from the core and very steep W density gradients in vicinity to the separatrix, the temperature screening is still present for He but it is too small ( $v_{\text{He}} < 0.1 \text{ m s}^{-1}$ ) to have a noticeable effect on the He transport in the core.

As a result, the core He density (shown in figure 20) is slightly peaked due to the He source originating from the fusion reactions taking place in the core. Moreover, although the main ion density profile is flat in the ETB region, an edge pedestal develops in the He density, which can also be explained by the location of the He source in the core. The average anomalous diffusivity is significantly larger for He (up to  $D_{\text{He}} \approx 5 \text{ m}^2 \text{ s}^{-1}$ ) compared to the main ions ( $D_{\text{D,T}} \leq 0.2 \text{ m}^2 \text{ s}^{-1}$ ) and it decreases towards the core in line with  $\chi_{i,e}$ . For this reason, the peaking in He density is very small ( $n_{\text{He}}(\rho=0)/n_{\text{He}}(\rho=1) \approx 1.3$ ) and essentially caused by increased He density gradients in the region close to the magnetic axis where the anomalous He transport is almost fully suppressed and He is transported due to sawteeth and neoclassical diffusion only. The He core concentration amounts to  $\sim 1.5\%$ , therefore the core dilution due to the He is negligible in this case. However, the He core concentration strongly depends on the He density and the He neutral influx at the separatrix, which has been prescribed and may have been underestimated.

According to equations (6) and (7) in [6],  $n_{\text{He}}$  in the range  $2\text{--}6 \cdot 10^{18} \text{ m}^{-3}$  and  $\Gamma_{\text{He}} \leq 2 \cdot 10^{20} \text{ s}^{-1}$  can be expected in this configuration. To test the effect of these parameters on the results, a second simulation was performed imposing  $n_{\text{He}} = 6 \cdot 10^{18} \text{ m}^{-3}$  and  $\Gamma_{\text{He}} = 2 \cdot 10^{20} \text{ s}^{-1}$  at the separatrix. The results are also reported in table 16 (case B). One can see that the He concentration is increased to  $\sim 5\text{--}7\%$ . However,

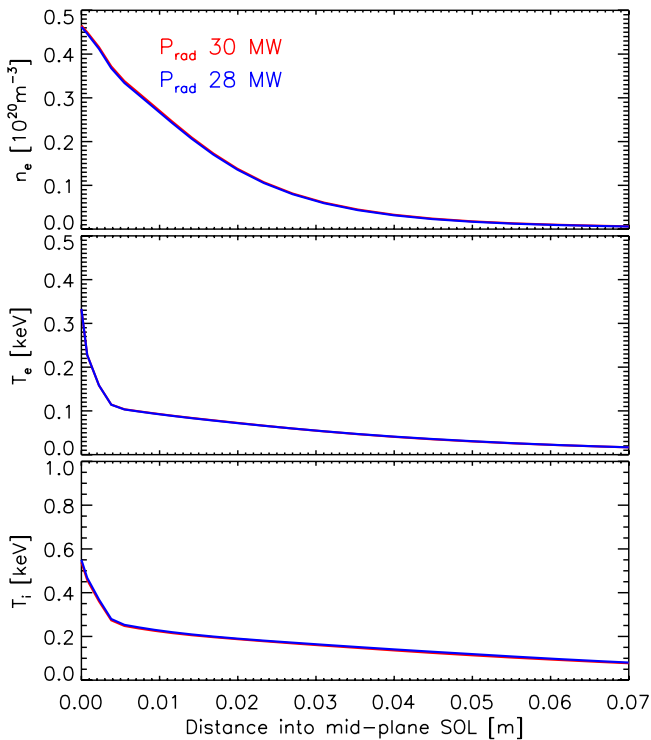


**Figure 21.** He accumulation with Ne seeding and pellet fuelling (section 6.6). Mid-plane SOL electron density and electron and ion temperature profiles for case A (red) and B (blue) in table 17.  $I_p = 15$  MA,  $B_T = 5.3$  T,  $P_{aux} = 53$  MW, with Ne seeding.

the effect on the dilution is marginal even in this case: compared to the simulation at  $n_{He} = 5 \cdot 10^{17} \text{ m}^{-3}$ ,  $P_{fus}$  is reduced from  $\sim 450$  MW to  $\sim 400$  MW. Due to profile stiffness, the He density profile is increased everywhere by  $5.5 \cdot 10^{18} \text{ m}^{-3}$  and the peaking is reduced to  $n_{He}(\rho = 0)/n_{He}(\rho = 1) \approx 1.07$ .

The anomalous He core transport is further enhanced reaching maximum diffusivities of  $D_{He} \approx 8 \text{ m}^2 \text{ s}^{-1}$ . This strong predicted level of He transport is the main reason why, even in this extreme conditions of low D-T throughput, fuelling by gas only and taking into account the stabilizing effect of the rotational shear, He ash contamination of the core plasma remains tolerable and the modelling results suggest that it may be possible to keep He accumulation in the core at an acceptable level in ITER baseline scenario configurations with gas fuelling only also at low D-T gas rates.

#### 6.6. Results 15 MA/5.3T/53 MW. He accumulation with pellet fuelling

The JINTRAC simulations for gas and pellet fuelled high  $Q$  H-mode plasmas at 15 MA, 5.3 T and 53 MW of auxiliary heating power (33 MW NBI and 20 MW ECRH) with W target presented previously have been repeated at a fixed D-T gas puff rate of  $1.0 \cdot 10^{22} \text{ s}^{-1}$  with Ne seeding. The He and Ne transport was taken into account and the Ne seeding was adjusted in order to provide a Ne radiation level in the SOL of  $\sim 30$  MW. Pellets are modelled with the HPI2 code with pellet size  $m_p = 5.5 \cdot 10^{21}$  atoms, velocity  $v_p = 300 \text{ m s}^{-1}$ , 50–50 D-T mixture and injection from the upper HFS. The

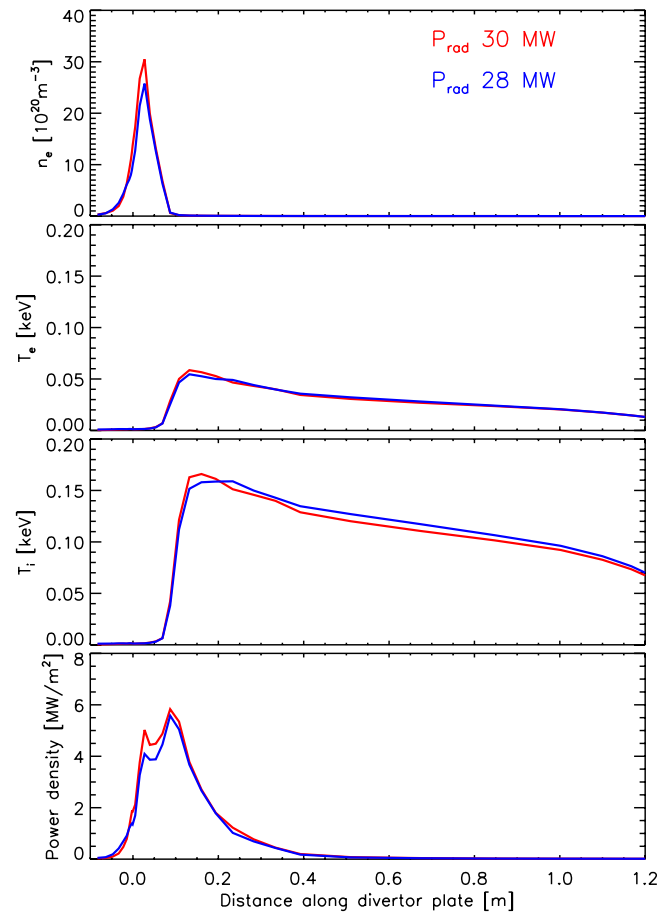


**Figure 22.** He accumulation with Ne seeding and pellet fuelling (section 6.6). Outer divertor target electron density, electron and ion temperature and power density profiles for case A (red) and B (blue) in table 17.  $I_p = 15$  MA,  $B_T = 5.3$  T,  $P_{aux} = 53$  MW, with Ne seeding.

pellet injection frequency is adjusted in order to maintain a line-averaged electron density of  $1.0 \cdot 10^{20} \text{ m}^{-3}$ . The He is produced due to the fusion reactions in the core. The simulation is continued for several tens of seconds until stationary conditions are approached for the He density in the core and edge regions.

The main simulation results are summarized in table 17. In figure 21 we show the electron density and electron and ion temperature profiles in the outer mid-plane SOL, whereas in figures 22 and 23 we show the electron density, electron and ion temperature and power density profiles at outer and inner divertor target, respectively. According to simulation results, the maximum power density on the inner and outer targets can be maintained below  $10 \text{ MW m}^{-2}$  with the applied D-T and Ne puff rates. To achieve a Ne radiation level in the SOL of  $\sim 30$  MW, an average Ne seeding rate of  $\sim 1.0 \cdot 10^{19} \text{ s}^{-1}$  is necessary. The ion temperature can be kept below the guideline level for W sputtering by light impurities of  $\sim 5 \text{ eV}$  in a region approximately 5 cm wide near the strike-point location on the outer target where the absolute ion current density peak is located. To maintain the density at a level of  $\sim 85\%$  of the Greenwald density limit, pellets with the standard ITER size need to be injected at a time-averaged frequency

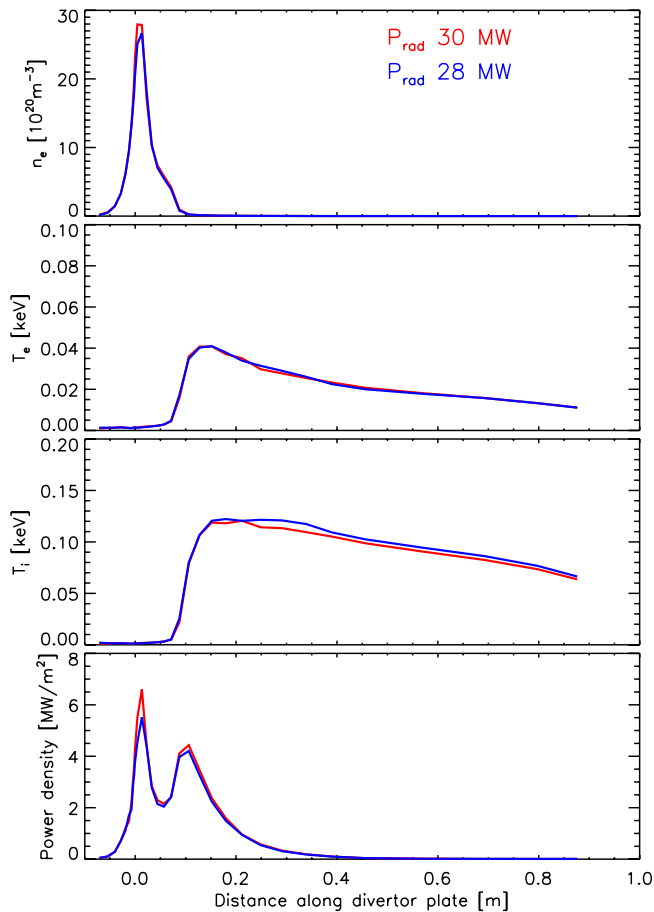


**Figure 23.** He accumulation with Ne seeding and pellet fuelling (section 6.6). Inner divertor target electron density, electron and ion temperature and power density profiles for case A (red) and B (blue) in table 17.  $I_p = 15$  MA,  $B_T = 5.3$  T,  $P_{\text{aux}} = 53$  MW, with Ne seeding.

of  $\sim 2$ – $2.5$  Hz which is in line with previous core transport fuelling studies presented in [34].

The He density at the separatrix saturates at  $\sim 2.5 \cdot 10^{18} \text{ m}^{-3}$  (4%–5% of the electron density at the separatrix), while the He density on axis approaches  $\sim 6 \cdot 10^{18} \text{ m}^{-3}$  (4%–5% of the on-axis electron density), corresponding to a core He peaking factor of  $\sim 2.4$ . This peaking factor is considerably larger than the one obtained in core-only simulations with GLF23 with comparable on-axis He density. This is due to differences in predictions for the He core diffusivity, which is assumed to be identical to the diffusivity for main ions with the modified Bohm/gyro-Bohm transport model and thus much lower than the  $D_{\text{He}}$  predicted by GLF23.

In quasi-stationary conditions the time-averaged He pump rate is identical to the He source rate due to fusion reactions in the core, which is  $\sim 1.75 \cdot 10^{20} \text{ s}^{-1}$ . As a consequence of increased plasma dilution, a slight degradation in fusion performance with respect to similar simulations without He from  $P_{\text{fus}} \approx 550$  MW to  $P_{\text{fus}} \approx 490$  MW is predicted, as the He concentration increases from  $\sim 2\%$  to  $\sim 4.5\%$ .  $Z_{\text{eff}} \approx 1.35$  in stationary conditions. Due to temperature screening in the edge region, the core Ne density can be kept at a comparably low level in the range  $2.5$ – $3.0 \cdot 10^{17} \text{ m}^{-3}$ , corresponding to a

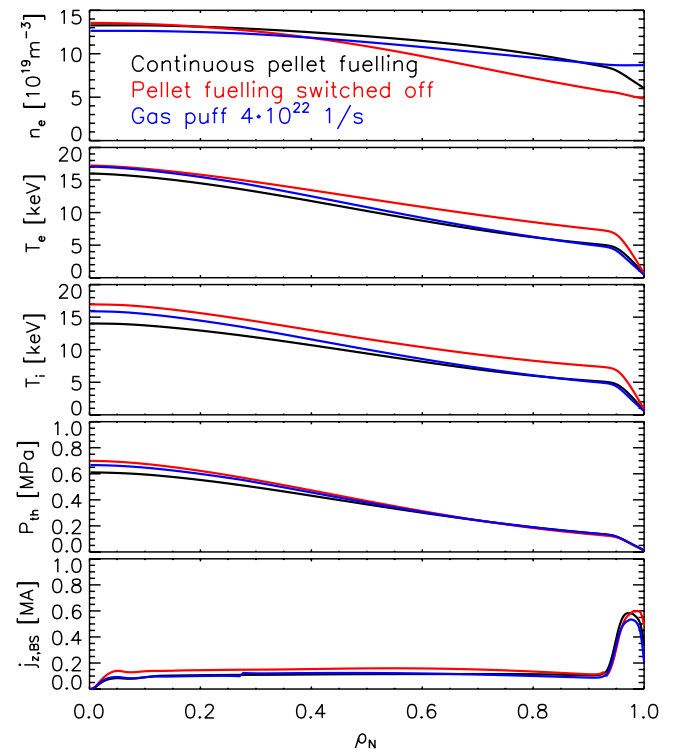


**Figure 24.** Electron density, electron temperature, ion temperature, thermal pressure and toroidal bootstrap current density profiles for three DT H-mode plasma simulations at 15 MA/5.3 T,  $P_{\text{aux}} = 53$  MW with W targets with pellet fuelling (red), with density decaying from stationary conditions with pellet fuelling to those with gas fuelling at low puff rates (red) and with strong gas fuelling  $\Gamma_{\text{D-T}} = 4 \cdot 10^{22} \text{ s}^{-1}$  (blue).

Ne core concentration of  $\sim 0.25\%$ . Without the edge temperature screening effect, the core Ne density could increase by  $\sim 1.0 \cdot 10^{17} \text{ m}^{-3}$  for the same Ne density at the separatrix. The total core radiation in stationary conditions amounts to  $\sim 25$  MW. Very similar results are obtained in another set of runs at a slightly reduced target Ne radiation in the SOL of  $\sim 28$  MW.

### 6.7. Results at 15 MA/5.3 T/53 MW. Sensitivity of bootstrap current density in pellet and gas fuelled plasmas

Differences in edge density and bootstrap current have been studied for full JINTRAC simulations of purely gas fuelled and pellet fuelled plasmas at 15 MA, 5.3 T and 53 MW of auxiliary power with W targets and Be from the wall included in the impurity mix. A comparison of plasma profiles is shown in figures 24 and 25 for three cases with continuous pellet fuelling, with pellet fuelling having been switched off before the start of the simulation and with a gas fuelling rate  $\Gamma_{\text{D-T}} = 4.0 \cdot 10^{22} \text{ s}^{-1}$ . The results of the simulations are summarized in table 18.

Although densities and temperatures are well comparable for the three cases in the core region, the edge densities deviate strongly. In the purely gas fuelled case, the density profile is almost flat in the ETB region which is due to negligible particle sources from the core, negligible particle pinch in the ETB and a very low flux of neutrals crossing the separatrix. For the pellet fuelled case however, a significant density

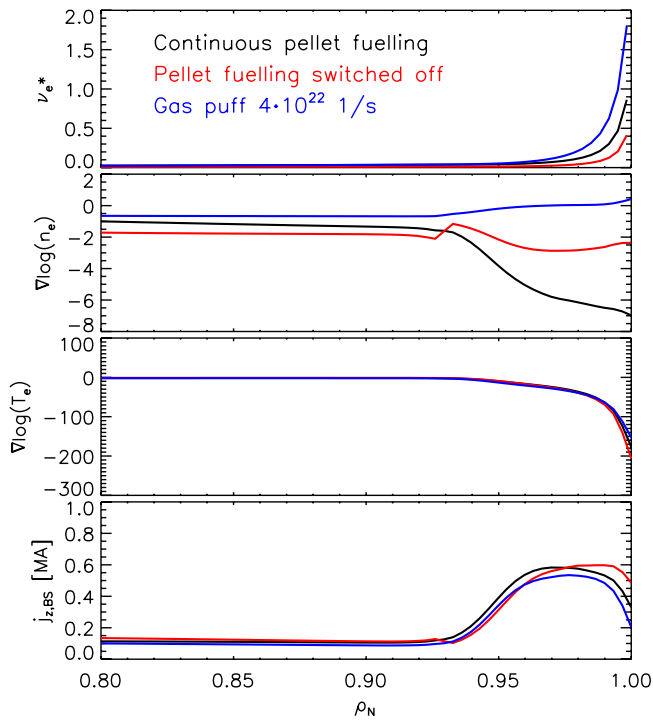


**Figure 25.** Profiles in the plasma edge region of normalized electron collisionality, logarithmic electron density derivative, logarithmic electron temperature derivative and bootstrap current density for three D-T H-mode plasma simulations at 15 MA/5.3 T,  $P_{\text{aux}} = 53$  MW with W targets with pellet fuelling (black), with density decaying from stationary conditions with pellet fuelling to those for gas fuelling at low gas fuelling rates (red) and with strong gas fuelling  $\Gamma_{\text{D-T}} = 4 \cdot 10^{22} \text{ s}^{-1}$  (blue).

gradient is predicted to appear in the ETB as a consequence of low particle diffusivity and a significant core particle source due to pellet fuelling. Due to these differences in density gradient, one would expect deviations in bootstrap current densities that could affect pedestal stability, as the influence of the density gradient on the bootstrap current density dominates that of the electron and ion temperatures for similar values of density and temperature logarithmic gradients. However, for the three cases analysed, the variation in bootstrap current is rather small.

The bootstrap current density,  $j_{\text{bs}}$ , has been predicted by the NCLASS model. Despite small deviations in the order of  $\sim 20\%$  in edge bootstrap current density, the predictions for  $j_{\text{bs}}$  do not appear to be in contradiction with the expression for  $j_{\text{bs}}$  given in [35]. Although  $dn_i/d\rho$  is reduced to zero in the case with strong gas fuelling and the collisionality is considerably increased due to higher densities in the ETB causing a reduction in bootstrap current, only a slight decrease in bootstrap current density can be expected compared to the case with pellet fuelling, as the terms proportional to the temperature gradients are dominant in these situations. As shown in figure 25, the logarithmic derivative of the electron temperature is up to two orders of magnitude larger than that of the electron density. It should be noted that the density at the separatrix is rather high for the case with pellet fuelling ( $\sim 6 \cdot 10^{19} \text{ m}^{-3}$ ) compared to typical configurations with

pellet fuelling, which is related to a rather low impurity contamination in the edge ( $Z_{\text{eff}} < 1.1$ ).

For higher impurity concentrations and lower density at the separatrix, the density gradient in the ETB is expected to increase by a factor  $\sim 2.0$ . The difference in bootstrap current density for purely gas fuelled and pellet fuelled configurations might then become more important, although the temperature gradient driven bootstrap current is likely to remain dominant. It is worth noting that in these simulations the critical pressure gradient at the pedestal ( $\alpha_c$ ) is assumed to be the same and independent of the separate contribution of the density and temperature gradients to the total pressure gradient in the pedestal and thus to the small changes of the bootstrap current discussed above. Given the fact that the contribution to the pressure gradient is dominated by the temperature gradient for both pellet fuelled and gas fuelled plasmas, as shown in figure 25, and that the resulting bootstrap current is similar, it is justified to assume that edge MHD stability both for gas fuelled and pellet fuelled plasmas in ITER that have a separatrix density high enough to ensure acceptable power fluxes at the divertor. Deviations from this ideal MHD framework could occur if edge transport were strongly dependent on the magnitude of the pedestal density gradients in these ITER conditions as this could affect the maximum pressure gradient that can be achieved and the pedestal width itself. Assessing such effects requires complex gyrokinetic simulations of edge plasma turbulent transport which are beyond the scope of this study.

#### 6.8. Results 15 MA/5.3 T/53 MW sensitivity to MHD peeling-ballooning stability limit ( $\alpha_c$ )

To investigate the sensitivity of the simulation results obtained with full JINTRAC to the assumptions for the pedestal width and ETB transport, scans have been carried out for purely gas fuelled D-T H-mode plasmas at 15 MA, 5.3 T, and 53 MW of auxiliary heating power with W target for high and medium gas puff rates of  $\Gamma_{\text{D-T}} = 1.0 \cdot 10^{22} \text{ s}^{-1}$  and  $\Gamma_{\text{D-T}} = 2.5 \cdot 10^{22} \text{ s}^{-1}$ .

In this series of simulations, instead of prescribing the ETB width according to the EPED1 model predictions (as it was done in most of the simulations presented in this paper), we varied it in order to scan the location of the top of the pedestal in the range between  $\rho = 0.91$  and  $\rho = 0.95$ , while the maximum allowed normalized pressure gradient in the ETB (which is controlled by the continuous ELM model) was increased from  $\alpha_c = 1.38$  to  $\alpha_c = 3.20$  in order to maintain the pressure at the top of the ETB around  $\sim 130$  kPa. In this way, the uncertainty in predictions for plasma confinement and fusion performance due to uncertainties in the pedestal width for a given pedestal pressure can be estimated. The results for the two levels of gas rate are summarized in tables 19 and 20.

For the range of  $\alpha_c$  and ETB width at constant pedestal pressure investigated, a variation in fusion power of  $\sim 200$  MW was found for both scans at low and medium gas puff rates. For the scan at  $\Gamma_{\text{D-T}} = 1.0 \cdot 10^{22} \text{ s}^{-1}$ ,  $Q$  varies between 8.5 and 12.5 while, at  $\Gamma_{\text{D-T}} = 2.5 \cdot 10^{22} \text{ s}^{-1}$ ,  $Q$  varies between 10.0 and 14.0. It should be noted that the impurity concentration

**Table 18.** Summary of results from section 6.7 (sensitivity of bootstrap current). Main plasma parameters achievable under different edge plasma kinetic profiles and bootstrap current in an ITER D-T H-mode plasma at 15 MA/5.3 T and 53 MW of additional power.

Case	A	B	C
$P_{\text{NBI}}/P_{\text{ECRH}}/P_{\text{ICRH}}$ (MW)	33/20/–	33/–/20	33/–/20
$\Gamma_{\text{D-T}} (10^{22} \text{ s}^{-1})/\Gamma_{\text{Ne}} (10^{20} \text{ s}^{-1})$	–/–	–/–	4.0/–
$\rho_{\text{p}}/\Delta_{\text{p}}/\Gamma_{\text{p}} (10^{21} \text{ s}^{-1})$	0.85/0.2/12.0	–	–
$f_{\text{G}}$	0.90	0.75	0.87
$H_{98}$	0.87	0.98	0.87
$n_{\text{e}}(0)/\langle n_{\text{e}} \rangle/n_{\text{e,sep}} (10^{19} \text{ m}^{-3})$	13.2/10.4/5.6	13.7/9.1/4.7	12.4/10.2/8.6
$T_{\text{e}}(0)/\langle T_{\text{e}} \rangle$ (keV)	16.0/8.2	17.2/10.2	17.1/8.5
$T_{\text{i}}(0)/\langle T_{\text{i}} \rangle$ (keV)	14.0/7.7	17.0/9.9	15.9/8.1
$P_{\text{fus}}$ (MW)/ $Q$	460.7/8.7	585.9/11.1	608.2/11.5
Divertor material	W	W	W
$Z_{\text{eff}}$	1.26	1.48	1.01
$P_{\text{IT}}/P_{\text{OT}}$ (MW $\text{m}^{-2}$ )	24.6/37.8	11.7/23.0	8.6/8.1
$P_{\text{sep}}/P_{\text{rad,core}}/P_{\text{rad,div}}$ (MW)	104.1/2.3/4.6	98.8/2.3/31.5	146.8/0.3/0.8

**Table 19.** Summary of results from section 6.8 (sensitivity to  $\alpha_{\text{c}}$  and ETB width, low gas rate). Main plasma parameters achievable for different ETB width and normalized critical pressure gradient  $\alpha_{\text{c}}$  assumptions in an ITER D-T H-mode plasma at 15 MA/5.3 T and 53 MW of additional power.

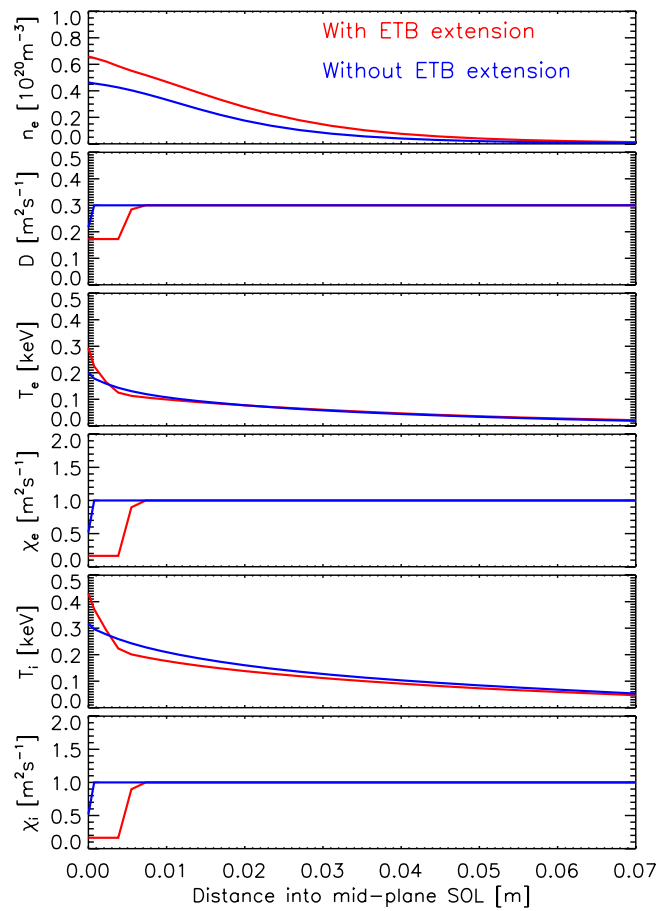
Case	A	B	C
$P_{\text{NBI}}/P_{\text{ECRH}}/P_{\text{ICRH}}$ (MW)	33/–/20	33/–/20	33/–/20
$\Gamma_{\text{D-T}} (10^{22} \text{ s}^{-1})/\Gamma_{\text{Ne}} (10^{20} \text{ s}^{-1})$	1.0/–	1.0/–	1.0/–
$f_{\text{G}}$	0.56	0.71	0.82
$H_{98}$	0.90	0.89	0.90
$n_{\text{e}}(0)/\langle n_{\text{e}} \rangle/n_{\text{e,sep}} (10^{19} \text{ m}^{-3})$	8.2/6.6/5.6	10.3/8.4/7.0	11.5/9.5/7.8
$T_{\text{e}}(0)/\langle T_{\text{e}} \rangle$ (keV)	20.0/10.7	18.7/9.8	18.2/9.4
$T_{\text{i}}(0)/\langle T_{\text{i}} \rangle$ (keV)	19.9/10.2	17.8/9.3	17.1/8.9
$P_{\text{fus}}$ (MW)/ $Q$	426.2/8.04	534.2/10.08	630.5/11.90
Divertor material	W	W	W
$Z_{\text{eff}}$	1.01	1.01	1.01
$P_{\text{IT}}/P_{\text{OT}}$ (MW $\text{m}^{-2}$ )	20.0/15.5	29/16.0	38.5/18.3
$P_{\text{sep}}/P_{\text{rad,core}}/P_{\text{rad,div}}$ (MW)	123.9/0.1/0.3	142.2/0.1/0.2	153.7/0.2/1.7
$\rho_{\text{ETB}}/\alpha_{\text{c}}$	0.91/1.38	0.93/1.9	0.95/3.2

**Table 20.** Summary of results from section 6.8 (sensitivity to  $\alpha_{\text{c}}$  and ETB width, medium gas rate). Main plasma parameters achievable for different ETB width and normalized critical pressure gradient  $\alpha_{\text{c}}$  assumptions in an ITER D-T H-mode plasma at 15 MA/5.3 T and 53 MW of additional power.

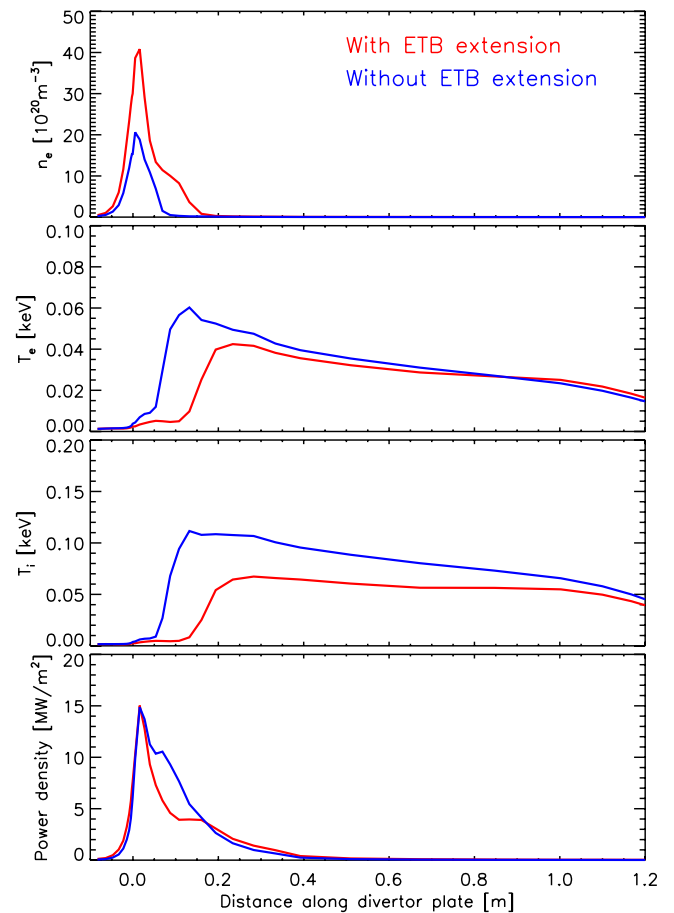
Case	A	B	C
$P_{\text{NBI}}/P_{\text{ECRH}}/P_{\text{ICRH}}$ (MW)	33/–/20	33/–/20	33/–/20
$\Gamma_{\text{D-T}} (10^{22} \text{ s}^{-1})/\Gamma_{\text{Ne}} (10^{20} \text{ s}^{-1})$	2.5/–	2.5/–	2.5/–
$f_{\text{G}}$	0.82	0.90	1.00
$H_{98}$	0.84	0.86	0.88
$n_{\text{e}}(0)/\langle n_{\text{e}} \rangle/n_{\text{e,sep}} (10^{19} \text{ m}^{-3})$	11.8/9.7/8.2	12.7/10.5/8.8	14.3/11.8/9.9
$T_{\text{e}}(0)/\langle T_{\text{e}} \rangle$ (keV)	17.0/8.4	17.1/8.4	17.0/8.4
$T_{\text{i}}(0)/\langle T_{\text{i}} \rangle$ (keV)	16.0/8.0	15.8/8.0	15.7/8.0
$P_{\text{fus}}$ (MW)/ $Q$	538.1/10.15	626.4/11.82	762.6/14.39
Divertor material	W	W	W
$Z_{\text{eff}}$	1.00	1.00	1.01
$P_{\text{IT}}/P_{\text{OT}}$ (MW $\text{m}^{-2}$ )	14.0/8.7	16.0/9.0	24.0/12.5
$P_{\text{sep}}/P_{\text{rad,core}}/P_{\text{rad,div}}$ (MW)	142.4/0.1/0.3	154.7/0.1/0.3	178.1/0.2/4.3
$\rho_{\text{ETB}}/\alpha_{\text{c}}$	0.91/1.38	0.93/1.9	0.95/3.2

**Table 21.** Summary of results from section 6.9 (effect of the extension of the ETB in the SOL). Main plasma parameters achievable with and without extension of reduced transport to the SOL in an ITER D-T H-mode plasma at 15 MA/5.3 T and 53 MW of additional power.

Case	A	B	C	D
$P_{\text{NBI}}/P_{\text{ECRH}}/P_{\text{ICRH}}$ (MW)	33/-/20	33/-/20	33/-/20	33/0/20
$\Gamma_{\text{D-T}} (10^{22} \text{ s}^{-1})/\Gamma_{\text{Ne}} (10^{20} \text{ s}^{-1})$	1.0/-	1.0/-	2.0/-	3.0/-
$f_{\text{G}}$	0.67	0.50	0.73	0.82
$H_{98}$	0.89	0.93	0.88	0.86
$n_e(0)/\langle n_e \rangle/n_{e,\text{sep}} (10^{19} \text{ m}^{-3})$	9.7/8.0/5.9	7.5/6.0/4.9	10.6/8.7/7.1	11.9/9.8/7.8
$T_e(0)/\langle T_e \rangle$ (keV)	19.0/9.9	21.0/11.8	18.0/9.3	17.1/8.6
$T_i(0)/\langle T_i \rangle$ (keV)	18.2/9.4	21.4/11.2	17.1/8.8	16.0/8.1
$P_{\text{fus}} (MW)/Q$	491.1/9.27	408.8/7.71	516.2/9.74	553.9/10.45
Divertor material	W	W	W	W
$Z_{\text{eff}}$	1.01	1.01	1.01	1.01
$P_{\text{IT}}/P_{\text{OT}} (MW \text{ m}^{-2})$	21.5/15.0	11.0/14.8	10.0/14.0	12.0/9.0
$P_{\text{sep}}/P_{\text{rad,core}}/P_{\text{rad,div}} (MW)$	130.4/0.1/0.4	120.6/0.1/0.2	137.3/0.1/0.4	127.8/0.1/0.4
ETB extension in the SOL (mm)	6.0	0.0	0.0	0.0

**Figure 26.** Mid-plane SOL electron density, particle diffusivity, electron temperature, electron heat conductivity, ion temperature and ion heat conductivity profiles for case A (red) and B (blue) in table 21.  $I_p = 15$  MA,  $B_T = 5.3$  T,  $P_{\text{aux}} = 53$  MW.

in these plasmas is very low with  $Z_{\text{eff}} \sim 1.01$ . This is a consequence of considering W targets without taking into account at the same time W sputtering and transport, not taking into account the presence of He, a negligible Be sputtering at the walls and no Ne seeding, all of which imply that, in the modelling, very high densities can be achieved with gas fuelling only. As a result of this artificial low radiation regime, none of the

**Figure 27.** Outer divertor target electron density, electron and ion temperature and power density profiles for case A (red) and B (blue) in table 21.  $I_p = 15$  MA,  $B_T = 5.3$  T,  $P_{\text{aux}} = 53$  MW.

plasma conditions simulated result in acceptable power fluxes at the ITER divertor.

Differences in fusion performance can be attributed to differences in predictions for the separatrix density that determines the level of core density and influences the fusion reaction rate in the core, which scales as  $n_D n_T$ . For both scans at low and medium gas puff rates, the variations of the density

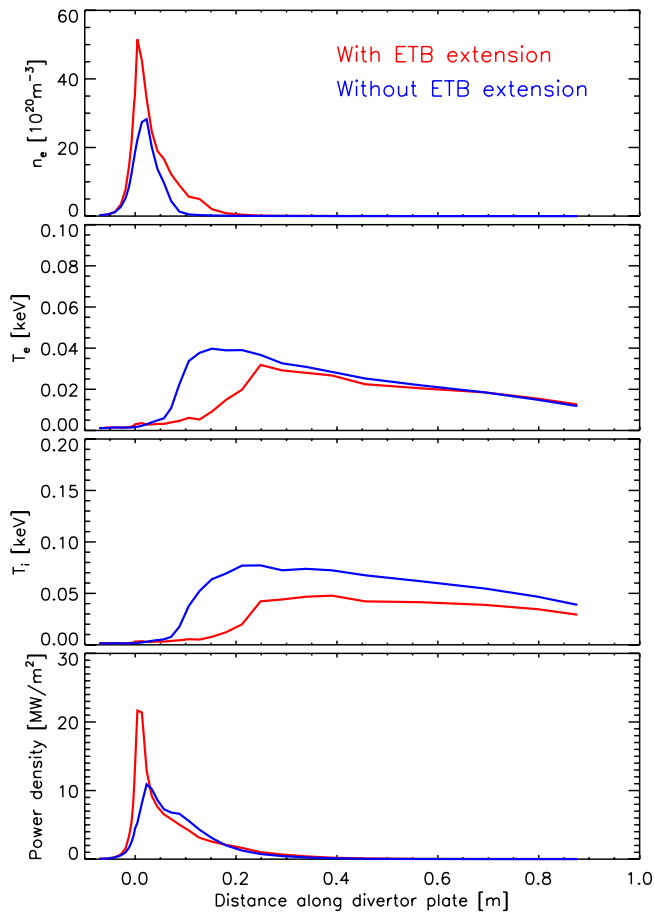


**Figure 28.** Inner divertor target electron density, electron and ion temperature and power density profiles for case A (red) and B (blue) in table 21.  $I_p = 15$  MA,  $B_T = 5.3$  T,  $P_{aux} = 53$  MW.

at the separatrix is in the range  $2.0\text{--}2.2 \cdot 10^{19} \text{ m}^{-3}$ . This variation is related to a change in transport coefficients in the near SOL, as the latter are determined by the transport coefficients applied in the ETB. The higher  $\alpha_c$  in the ETB, the lower become the continuous ELM model predictions for  $D$ ,  $\chi_e$  and  $\chi_i$ , as lower transport coefficients are required to maintain a higher pedestal pressure in the ETB. As diffusion in the near SOL is reduced with lower  $D$ ,  $\chi_e$  and  $\chi_i$ , the density and temperature gradients in that region are increased and higher separatrix densities are achieved for higher  $\alpha_c$ .

It should be pointed out that the predicted variation in the density at the separatrix and the associated change in fusion performance seems to be almost entirely due to the assumption that the ETB transport is extended by a few millimetres into the SOL. Without this assumption, the transport in the near SOL would not be affected by a variation in  $\alpha_c$  or in the ETB width, the density in the near SOL would remain similar, and thus similar separatrix density and fusion power predictions would be obtained. A sensitivity scan with respect to the ETB extension into the SOL will be presented in the next subsection.

It is also worth noting that the simulation assumptions for the scans in  $\alpha_c$  are questionable not only with respect to impurity contamination but also in view of divertor conditions. The limit of  $10 \text{ MW m}^{-2}$  is exceeded for all cases at low and

medium gas puff rate at least on one target plate, as the total heat flux from the core is very large and no Ne seeding has been applied. However, the ion temperature near the strike point locations can be maintained below the guideline level of 5 eV for W sputtering by light impurities at least for the cases at  $\Gamma_{D-T} = 2.5 \cdot 10^{22} \text{ s}^{-1}$ .

### 6.9. Results at 15 MA/5.3 T/53 MW. Sensitivity to ETB extension in the SOL

As mentioned above, the assumption of an extension of the ETB into the SOL can be expected to have a strong influence on predicted plasma conditions. To test the sensitivity of the results to this assumption, we carried out a scan of the width of the ETB extension into the SOL, based on the full JINTRAC simulations of purely gas fuelled D-T H-mode plasmas at 15 MA, 5.3 T, 53 MW of auxiliary heating power and with W targets. The results are summarized in table 21, where simulation results are shown for a case with an ETB extension into the SOL of  $\sim 6$  mm on the outer mid-plane (which is the standard assumption for all H-mode plasma simulations presented in this paper) at a low D-T gas puff rate of  $\Gamma_{D-T} = 1.0 \cdot 10^{22} \text{ s}^{-1}$ , and for cases without an ETB extension into the SOL at fixed D-T gas puff rates of  $\Gamma_{D-T} = 1.0 \cdot 10^{22} \text{ s}^{-1}$ ,  $\Gamma_{D-T} = 2.0 \cdot 10^{22} \text{ s}^{-1}$  and  $\Gamma_{D-T} = 3.0 \cdot 10^{22} \text{ s}^{-1}$ . No Ne seeding was used in these simulations. As a consequence, the impurity concentration was very low, resulting in  $Z_{eff} \approx 1.0$ . In figure 26 we show the electron density, particle diffusivity, electron temperature, electron heat conductivity, ion temperature and ion heat conductivity profiles at the outer mid-plane for the cases with and without ETB extension in the SOL with fixed  $\Gamma_{D-T} = 1.0 \cdot 10^{22} \text{ s}^{-1}$ . In figures 27 and 28 we show the electron density, electron and ion temperature and power density profiles for the same two cases on the outer and inner divertor, respectively.

As expected, the predicted plasma performance is significantly affected by the assumption of an ETB extension of a few millimetres into the SOL. For two cases at low gas puff rate with and without ETB extension, the predicted fusion power varies by  $\sim 80$  MW. Without ETB extension,  $Q \approx 7.7$ , while with an ETB extension of  $\sim 6$  mm  $Q \approx 9.2$  is obtained. Similarly to the scan in ETB width presented in the previous subsection, the change in plasma performance is directly linked to a change in density at the separatrix, which largely determines the density in the core and thus the fusion reaction rate. Without a reduction of the transport extended from the ETB into the near SOL, the transport coefficients prescribed for the far SOL are applied everywhere in the SOL up to the separatrix. These transport coefficients are much larger than those predicted for the ETB region with the continuous ELM model. For this reason, the temperature and density gradients in the near SOL are reduced without ETB extension compared to the case with an ETB extension. As for the density, this effect is comparably small. The jump in density over the first  $\sim 5$  mm in the near SOL on the outer mid-plane is only changed from  $\sim 0.75 \cdot 10^{19} \text{ m}^{-3}$  to  $\sim 1.5 \cdot 10^{19} \text{ m}^{-3}$  with application of an ETB extension. On the other hand the jump in temperature increases from  $\sim 50$  eV to  $\sim 300$  eV. Consequently, with much

**Table 22.** Summary of results from section 6.10 (sensitivity to transport coefficients in the SOL). Main plasma parameters achievable for different gas fuelling rates and transport in the SOL fixed as in [8] in an ITER D-T H-mode plasma at 15 MA/5.3 T and 53 MW of additional power.

Case	A	B	C
$P_{\text{NBI}}/P_{\text{ECRH}}/P_{\text{ICRH}}$ (MW)	32/–/20	33/–/20	33/–/20
$\Gamma_{\text{D-T}} (10^{22} \text{ s}^{-1})/\Gamma_{\text{Ne}} (10^{20} \text{ s}^{-1})$	1.0/–	2.0/–	3.0/–
$f_G$	0.50	0.73	0.84
$H_{98}$	0.93	0.88	0.86
$n_e(0)/\langle n_e \rangle/n_{e,\text{sep}} (10^{19} \text{ m}^{-3})$	7.4/6.0/4.9	10.5/8.6/7.1	12.2/10.0/8.3
$T_e(0)/\langle T_e \rangle$ (keV)	21.0/11.8	18.0/9.3	17.0/8.6
$T_i(0)/\langle T_i \rangle$ (keV)	21.4/11.2	17.1/8.8	16.0/8.1
$P_{\text{fus}} \text{ (MW)}/Q$	408.8/7.71	516.2/9.74	579.6/10.94
Divertor material	W	W	W
$Z_{\text{eff}}$	1.01	1.01	1.01
$P_{\text{IT}}/P_{\text{OT}} \text{ (MW m}^{-2}\text{)}$	11.0/14.9	10.4/14.1	12.1/10.2
$P_{\text{sep}}/P_{\text{rad,core}}/P_{\text{rad,div}} \text{ (MW)}$	120.6/0.1/0.2	137.3/0.1/0.4	149.8/0.1/0.4

higher temperatures near the separatrix on the outer mid-plane, the plasma energy is also considerably enhanced near the strike-point positions on the target plates, where the recycling process is localized. Due to the higher plasma pressure in this region, recycled neutrals are more likely to be ionized again, and a lower amount of recycled neutrals can escape the divertor plasma. For this reason the overall plasma density in the SOL and the divertor is increased compared to the case without ETB extension in stationary conditions for the same gas puff rates and approximately identical pump rates. As the parallel heat flux decay length  $\lambda_q$  is reduced for reduced transport coefficients in the near SOL with an ETB extension into the SOL, the power is deposited on the target plates in a narrower region near the strike-point location. For this reason, the maximum power density on the target plates is considerably larger if an ETB extension is taken into account. It should be noted that for all cases modelled the divertor power fluxes exceed  $10 \text{ MW m}^{-2}$ , as no Ne is injected in these simulations.

Applying a scan in gas puff rates with zero ETB extension into the SOL, similar variations in fusion power and density are achieved as for a scan in  $\Gamma_{\text{D-T}}$  with non-zero ETB extension, however, low temperature divertor conditions are achieved at lower  $\Gamma_{\text{D-T}}$  and separatrix densities. As can be seen from table 21, the increase in density for cases with  $\Gamma_{\text{D-T}} = 3.0 \cdot 10^{22} \text{ s}^{-1}$  with respect to cases with  $\Gamma_{\text{D-T}} = 2.0 \cdot 10^{22} \text{ s}^{-1}$  is reduced compared with the increase between cases with  $\Gamma_{\text{D-T}} = 2.0 \cdot 10^{22} \text{ s}^{-1}$  and  $\Gamma_{\text{D-T}} = 1.0 \cdot 10^{22} \text{ s}^{-1}$ . This is an indication that detached conditions are already approached at  $\Gamma_{\text{D-T}} = 3.0 \cdot 10^{22} \text{ s}^{-1}$ . A similar reduction of the density increment was observed for the same scan with non-zero ETB extension around  $\Gamma_{\text{D-T}} = 4.0 \cdot 10^{22} \text{ s}^{-1}$ , as shown previously. Due to lower predicted separatrix densities with zero ETB extension for the same D-T gas puff rate,  $Q$  is reduced compared to similar plasma configurations with non-zero ETB extension. At the maximum applicable gas puff rates with zero ETB extension we obtain  $Q \leq 10$  even for a pure plasma with  $Z_{\text{eff}} \approx 1.0$ . At higher gas puff rates, it seems to be possible to keep the maximum power density below  $10 \text{ MW m}^{-2}$  and to maintain  $T_i < 5 \text{ eV}$  near the strike-point locations with zero ETB

extension into the SOL even for pure plasmas without Ne seeding (but neglecting W sputtering and transport) due to increased  $\lambda_q$  in this case compared with our standard assumption, but only at the outer divertor.

#### 6.10. Results at 15 MA/5.3 T/53 MW. Gas fuelling rate scan with fixed transport in the SOL

JINTRAC simulations of purely gas fuelled D-T H-mode plasmas at 15 MA, 5.3 T, auxiliary heating power 53 MW and with W targets have been repeated with the same assumptions for SOL transport as used in previous edge modelling studies for ITER as, for example, in [8]. In particular, fixed constant transport coefficients  $D = 0.3 \text{ m}^2 \text{ s}^{-1}$ ,  $\chi_e = \chi_i = 1.0 \text{ m}^2 \text{ s}^{-1}$  have been applied everywhere in the SOL. The D-T gas puff rate has been varied between  $1.0 \cdot 10^{22} \text{ s}^{-1}$  and  $3.0 \cdot 10^{22} \text{ s}^{-1}$ . Ne seeding was not applied. The results are summarized in table 22.

Simulation results and conclusions are comparable to those for the scan in gas puff rate at zero ETB extension presented previously, as transport coefficients in the SOL and other simulation conditions are very similar. The far SOL transport coefficients in the scan at zero ETB extension are the same as those applied everywhere in the SOL in this scan.

This scan provides an opportunity to do a closer comparison with predictions for similar ITER plasma configurations analysed in the past in simulations combining B2-EIRENE and ASTRA with the same SOL transport assumptions [5, 6]. In fact, the predictions for core fusion performance and power crossing the separatrix from the scan presented here deviate only slightly from the simulations described in [6] (auxiliary power 53 MW and  $\langle n_{\text{D-T}} \rangle$  in the range  $6\text{--}8 \cdot 10^{19} \text{ m}^{-3}$ ).

Indeed, more recent simulations with ASTRA including the self-consistent evaluation of the pedestal pressure from the EPED1 model and the SOL relations derived from B2-EIRENE in [6] found similar values of  $Q$  for the densities modelled with JINTRAC [12]. In addition, the SOL parameter relation for the maximum power density at the target plates (including power deposited by radiation and neutral

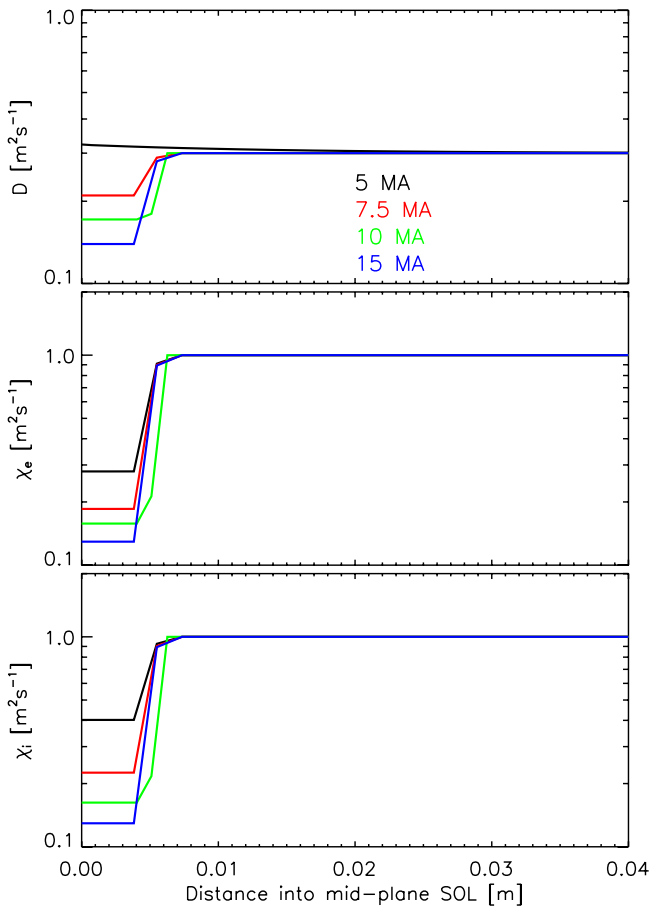


**Figure 29.** Particle diffusivity and electron and ion thermal conductivity profiles in the mid-plane SOL for different values of  $I_p$ . The simulations shown in the figure are case B in table 1 ( $I_p = 5$  MA,  $B_T = 5.3$  T,  $P_{aux} = 53$  MW), case B in table 2 ( $I_p = 7.5$  MA,  $B_T = 5.3$  T,  $P_{aux} = 53$  MW), case C in table 6 ( $I_p = 10$  MA,  $B_T = 5.3$  T,  $P_{aux} = 53$  MW) and case A in table 10 ( $I_p = 15$  MA,  $B_T = 5.3$  T,  $P_{aux} = 53$  MW).

interaction) given in equations (1) and (4) in [6] seems to apply quite well also to the cases considered here. The neutral influx at the separatrix is estimated to be  $\sim 1.0 \cdot 10^{21} \text{ s}^{-1}$  and in the same order of magnitude as that predicted by equation (5) in [6]. However, in absolute terms, the predicted main ion density at the separatrix is significantly higher in this scan than that given by equation (8) in [6]. According to equation (8), at the separatrix  $n_{D-T} \approx 4.0 \cdot 10^{19} \text{ m}^{-3}$  for a power in the SOL of  $\sim 120$  MW, whereas  $n_{D-T} \geq 5.0 \cdot 10^{19} \text{ m}^{-3}$  for this scan. It should be noted that from the point of view of divertor power load control, only the case at  $\Gamma_{D-T} = 3.0 \cdot 10^{22} \text{ s}^{-1}$  is marginally compatible with the requirement of maintaining the peak divertor heat flux under  $10 \text{ MW m}^{-2}$ .

Because of the discrepancy in the separatrix density in absolute terms, the same fusion performance can be obtained in the JINTRAC calculations at much lower particle source rates with gas fuelling only, whereas in [6] some pellet fuelling had to be considered to achieve high core densities at limited densities at the separatrix. The differences in separatrix densities are related to the impurity species and concentrations considered in the two simulations (in this scan only Be and Ne were considered, whereas in the B2-EIRENE/ASTRA

simulations the impurity mix included He, Be and C). Also, the different assumptions for the material of plasma facing components (Be and W in this scan and C in the B2-EIRENE/ASTRA simulations) could have had some influence on the results. In fact, the impurity concentration in this scan ( $Z_{eff} \leq 1.01$ ) is significantly lower compared to the simulations in [6] in which significant C sputtering is present and  $Z_{eff} \geq 1.7$  at the separatrix for a power in the SOL  $\sim 120$  MW, according to equations (6), (8) and (11) in [6].

The increased impurity content in the simulations leads to an increase of the radiation in the SOL by  $\sim 30$ – $40$  MW in the simulations in [6] compared to this scan, which leads to lower separatrix densities in the B2-EIRENE/ASTRA studies. Indeed, as already mentioned in [5] and in previous ITER edge modelling studies, simulations with low impurity content of ITER high  $Q$  scenarios would require very high separatrix densities to achieve divertor power load control. These were considered not to be compatible with high pedestal pressure or high energy confinement required for high  $Q$  in ITER on the assumption that the plasma behaviour observed in present experiments can be extrapolated to ITER, which as previously mentioned, remains to be proven.

Indeed, simulations with JINTRAC with Be divertor targets and low gas flux of  $\Gamma_{D-T} = 0.75 \cdot 10^{22} \text{ s}^{-1}$  (not shown in this paper) have a higher  $Z_{eff} \approx 1.7$ – $1.8$ , increased impurity radiation in the divertor and SOL and degraded fusion performance with a power in the SOL  $\sim 95$  MW. For such simulations, the main ion density at the separatrix dropped to lower values  $\sim 2.5 \cdot 10^{19} \text{ m}^{-3}$ , similar to those obtained for comparable conditions in [6]. Taking into account the discrepancies in impurity modelling assumptions, one can conclude that good overall agreement was found between independently performed JINTRAC and B2-EIRENE/ASTRA predictions for the 15 MA ITER baseline scenario core and edge Ne which strongly supports the validity of both of these integrated modelling approaches for stationary conditions.

## 7. Discussion

In the previous sections we have presented in detail simulations results for different fuelling, seeding and heating schemes for the flat-top of an ITER H-mode discharge at different plasma current and toroidal magnetic field.

The results show that, at 5 and 7.5 MA the fuelling of this phase of the discharge does not present particular problems. Densities above the limit required for unrestricted operation of the neutral beams with acceptable first wall shine-through loads can be maintained relatively easily by means of gas puff only and, because of the low fusion power generated in the plasma, the control of the power density on the divertor plates does not represent a problem either. These conclusions are not critically sensitive to the hypothesis we made on the transport in the ETB and the SOL.

The situation changes radically when we increase the plasma current to 10 and 15 MA. For these levels of plasma current the requirements on the density are more challenging (especially if one wants to achieve a relatively high  $Q$ ) and the

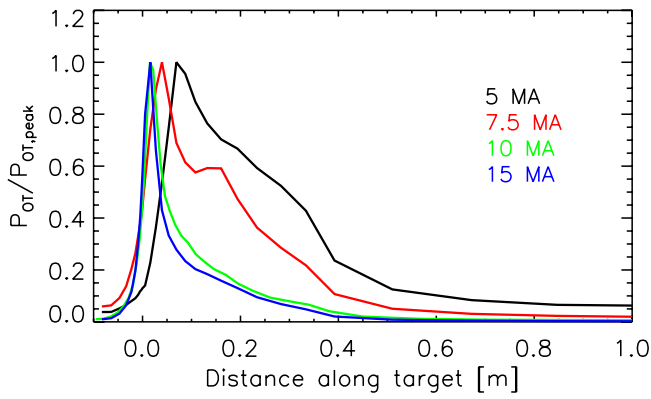


**Figure 30.** Outer divertor power density profiles normalized to the peak value. The simulations shown in the figure are the same as in figure 29.

increasing fusion power imposes an additional thermal load on the divertor.

An additional aspect highlighted by the fully integrated core/SOL simulations presented in this study is the scaling of the transport in the ETB with the plasma current and the effect that this has on the divertor. In fact, as we increase  $I_p$  and the pedestal pressure to reach the peeling-ballooning MHD limit, the transport in the ETB decreases and the power deposition profiles at the divertor become narrower. This, together with the increased fusion power generated at higher  $I_p$ , contributes to enhancing the power density on the divertor target. Quantitatively this is shown in figures 29 and 30, where we plot, for different values of  $I_p$ , the particle diffusivity and electron and ion thermal conductivity profiles in the mid-plane SOL and the power density profiles normalized to the peak value, respectively. It is worth noting that for all the simulations in the figures the fuelling rate was  $\Gamma_{D-T} = 1.0 \cdot 10^{22} \text{ s}^{-1}$  and the divertor was not approaching detachment.

As we have shown in the simulations presented in the previous sections the results depend crucially on the hypothesis made about the transport in the ETB and the SOL. In particular, if we assume that the transport is unaffected by the level of gas puff and the density at the separatrix is limited exclusively by the detachment of the divertor, we have shown that the required densities could be achieved by gas puff only. On the other hand, if we assume, as observed in present day experiments, that gas puffing degrades the confinement and enhances the transport at the plasma edge, then gas puff alone might not be sufficient to achieve the density required to sustain  $Q = 10$ .

In this case pellets will have to be used to fuel the discharge. Depending on the pellet mass, injection frequencies in the order of a few Hz are required. However, simulations show that, in certain conditions, too big pellets can cause perturbations of the separatrix density that can result in thermal instabilities and divertor detachment and threaten the stability of the discharge.

A further thermal stability aspect highlighted by the simulations at plasma current above 10 MA is the power load on the divertor targets due to the fusion power generated inside the plasma. We have shown that, without any mitigation

techniques, this can easily exceed the limit of  $10 \text{ MW m}^{-2}$ , which is the design maximum power flux for the ITER divertor. Moreover, the temperature in front of the divertor plates can exceed the limit of 5 eV, above which the sputtering of W by light impurities becomes possible.

Our simulations also show that optimization of the gas fuelling and Ne seeding is required to decrease the divertor power flux under  $10 \text{ MW m}^{-2}$  while maintaining an appropriately low level of core Ne concentration and associated core plasma radiation.

Finally, we would like to point out that there are additional aspects (not considered in this study) that could affect the results presented in this paper. In particular, in a mitigated ELM regime (for example by resonant magnetic perturbations) the normalized pressure gradient in the ETB  $\alpha_c$  could be lower than assumed in the simulations presented here, where the estimate of the pedestal pressure was based on unperturbed stability analysis. Moreover, in a mitigate ELM regime, one should expect a ‘density pump-out’ effect, which would likely affect the fuelling requirement for a given scenario [36]. The assessment of the impact of these phenomena on the simulations result is beyond the scope of this paper, since it is not clear at the moment how they could be included in the integrated scenario modelling.

## 8. Conclusions

In this paper we have analysed extensively the problem of fuelling the flat top of a range of ITER H-mode D-T plasma with plasma current from 5 to 15 MA with particular attention to the possibility of attaining densities compatible simultaneously with the unrestricted operation of the NBI (avoiding excessive shine-through loads on the first wall, especially at low plasma current and density), the reduction of the power density load on the divertor plates to below  $10 \text{ MW m}^{-2}$  and the achievement of fusion power in the order of 500 MW at 15 MA, resulting in  $Q = 10$ . In doing so we have conducted several sensitivity studies aimed at assessing the less known aspects of the problem, in particular the detail of the transport in the ETB and the SOL.

The results of the analysis indicate that, in principle, it is possible to fuel the burn phase of an ITER H-mode D-T plasma at 15 MA and achieve  $Q = 10$  and, at the same time, maintain the power load on the divertor below  $10 \text{ MW m}^{-2}$  by tuning the gas fuelling and the impurity seeding schemes to each particular scenario. The details of the fuelling, seeding and heating schemes to achieve these conditions have been described case by case. When simulations are performed in the same conditions, the results are in line with those of other approaches, in which the core plasma input into the edge plasma simulation codes is provided by boundary conditions [5–14].

As it is considered that the separatrix density or the density gradient in the pedestal compatible with good H-mode confinement can be restricted in ITER, pellet fuelling is used to achieve the required high core densities for high Q operation. In this case the transient perturbation induced by the

pellet injection should be limited in size in order to avoid total detachment of the divertor following pellet injection. Our simulations reveal that the inclusion of discrete pellet modelling in the simulations of  $Q = 10$  plasmas introduces further requirements for the optimization of the overall gas fuelling and impurity injection together with that of the average pellet fuelling and the size of the individual pellets injected.

A detailed analysis of transient phenomena and of the phases leading to and out of a steady-state H-mode in ITER (namely current ramp-up including H-mode access and ramp-down including exit from the H-mode) will be the subject of further publications.

## Acknowledgments

JINTRAC was used under licence agreement between Euratom and CCFE, Ref. Ares(2014)3576010-28/10/2014. This work was funded jointly by the RCUK Energy Programme (grant number EP/I501045) and by ITER Task Agreement C19TD51FE implemented by Fusion for Energy under Grant GRT-502. To obtain further information on the data and models underlying this paper, whose release may be subject to commercial restrictions, please contact PublicationsManager@ukaea.uk. The views and opinions expressed do not necessarily reflect those of Fusion for Energy which is not liable for any use that may be made of the information contained herein. The views and opinions expressed herein do not necessarily reflect those of the ITER Organization.

## ORCID iDs

L. Garzotti  <https://orcid.org/0000-0002-3796-9814>  
M. Valovič  <https://orcid.org/0000-0002-0855-1056>

## References

- [1] Kukushkin A.S. *et al* 2007 *Nucl. Fusion* **47** 698
- [2] Romanelli M. *et al* 2015 *Nucl. Fusion* **55** 093008
- [3] Militello Asp E. *et al* 2017 *Preprint: 2016 IAEA Fusion Energy Conf. (Kyoto, Japan, 17–22 October 2016)* ed R. Kaiser *et al* (Vienna: International Atomic Energy Agency) TH/P2-23 (<https://nucleus.iaea.org/sites/fusionportal/Shared%20Documents/FEC%202016/fec2016-preprints/preprint0255.pdf>)
- [4] Romanelli M. *et al* 2014 *Plasma Fusion Res.* **9** 3403023
- [5] Pacher G.W., Pacher H.D., Janeschitz G. and Kukushkin A.S. 2008 *Nucl. Fusion* **48** 105003
- [6] Pacher H.D., Kukushkin A.S., Pacher G.W., Kotov V. and Reiter D. 2011 *J. Nucl. Mater.* **415** S492
- [7] Pacher G.W. *et al* 2011 *Nucl. Fusion* **51** 083004
- [8] Kukushkin A.S., Pacher H.D., Pacher G.W., Kotov V., Pitts R.A. and Reiter D. 2013 *J. Nucl. Mater.* **438** S203
- [9] Kukushkin A.S. *et al* 2013 *Nucl. Fusion* **53** 123024
- [10] Kukushkin A.S., Polevoi A.R., Pacher H.D., Pacher G.W. and Pitts R.A. 2011 *J. Nucl. Mater.* **415** S497
- [11] Pacher H.D., Kukushkin A.S., Pacher G.W., Kotov V., Pitts R.A. and Reiter D. 2015 *J. Nucl. Mater.* **463** 591
- [12] Polevoi A.R. *et al* 2015 *Nucl. Fusion* **55** 063019
- [13] Polevoi A.R. *et al* 2017 *Nucl. Fusion* **57** 022014
- [14] Polevoi A.R. *et al* 2018 *Nucl. Fusion* **58** 056020
- [15] Houlberg W.A., Shaing K.C., Hirshman S.P. and Zarnstorff M.C. 1997 *Phys. Plasmas* **4** 3230
- [16] Erba M., Cherubini A., Parail V.V., Springmann E. and Taroni A. 1997 *Plasma Phys. Control. Fusion* **39** 261
- [17] Waltz R.E., Staebler G.M., Dorland W., Hammett G.W., Kotschenreuther K. and Konings J.A. 1997 *Phys. Plasmas* **4** 2482
- [18] Parail V. *et al* 2009 *Nucl. Fusion* **49** 075030
- [19] Garzotti L., Corrigan G., Heading D., Jones T.T.C., Parail V., Pégourié B. and Spence J. 2000 *27th European Physical Society Conf. on Plasma Physics (Budapest, Hungary, 12–16 June 2000)* (*Europhysics Conf. Abstracts* vol 24B) ed K. Szegő *et al* (Mulhouse: European Physical Society) p P1.078 ([http://epsppd.epfl.ch/Buda/pdf/p1\\_078.pdf](http://epsppd.epfl.ch/Buda/pdf/p1_078.pdf))
- [20] Snyder P.B., Groebner R.J., Hughes J.W., Osborne T.H., Beurskens M., Leonard A.W., Wilson H.R. and Xu X.Q. 2011 *Nucl. Fusion* **51** 103016
- [21] Groth M. *et al* 2011 *Plasma Phys. Control. Fusion* **53** 124017
- [22] Wiesen S., Fundamenski W., Wischmeier M., Groth M., Brezinsek S., Naulin V. and JET EFDA Contributors 2011 *J. Nucl. Mater.* **415** S535
- [23] Belo P. *et al* 2015 *42th European Physical Society Conf. on Plasma Physics (Lisbon, Portugal, 22–26 June 2015)* (*Europhysics Conf. Abstracts* vol 39E) ed R. Bingham *et al* (Mulhouse: European Physical Society) p P4.120 (<http://ocs.ciemat.es/EPS2015PAP/pdf/P4.120.pdf>)
- [24] Challis C.D., Cordey J.G., Hammen H., Stubberfield P.M., Christiansen J.P., Lazzaro E., Muir D.G., Stork D. and Thompson E. 1989 *Nucl. Fusion* **29** 563
- [25] Reiter D., Baelmans M. and Börner P. 2005 *Fusion Sci. Technol.* **47** 172
- [26] Pégourié B., Waller V., Nehme H., Garzotti L. and Géraud A. 2007 *Nucl. Fusion* **47** 44
- [27] Kukushkin A.S. *et al* 2007 *J. Nucl. Mater.* **363–5** 308
- [28] Singh M.J. *et al* 2017 *New J. Phys.* **19** 055004
- [29] Kallenbach A. *et al* 2005 *Plasma Phys. Control. Fusion* **47** B207
- [30] Kukushkin A.S. *et al* 2002 *Nucl. Fusion* **42** 187
- [31] Maget P., Artaud J.-F., Bécoulet M., Casper T., Faustin J., Garcia J., Huijsmans G.T.A., Loarte A. and Saibene G. 2013 *Nucl. Fusion* **53** 093011
- [32] Eich T. *et al* 2018 *Nucl. Fusion* **58** 034001
- [33] Eich T. *et al* 2013 *Nucl. Fusion* **53** 093031
- [34] Garzotti L., Belo P., Corrigan G., Köchl F., Lönnerth J., Parail V., Pereverzev G., Saarelma S., Tardini G. and Valovič M. 2012 *Nucl. Fusion* **52** 013002
- [35] Sauter O., Angioni C. and Lin-Liu Y.R. 1999 *Phys. Plasmas* **6** 2839
- [36] Valovič M. *et al* 2016 *Nucl. Fusion* **56** 066009